Gold Nanoparticle Uptake in Synchronized Cell Populations and the Effect on Radiation Sensitization

by

Kristy Rieck
B.Sc., University of Guelph, 2016

A Thesis Submitted in Partial Fulfillment
of the Requirements for the Degree of

MASTER OF SCIENCE

in the Department of Physics and Astronomy

Supervisory Committee

Gold Nanoparticle Uptake in Synchronized Cell Populations and the Effect on Radiation Sensitization

by

Kristy Rieck
B.Sc., University of Guelph, 2016

Supervisory Committee

Dr. Devika Chithrani, (Department of Physics and Astronomy)
Supervisor

Dr. Wayne Beckham, (Department of Physics and Astronomy)
Departmental Member

Dr. Isabelle Gagne, (Department of Physics and Astronomy)
Departmental Member

Abstract

To overcome the challenge in radiation therapy of delivering the prescribed dose to cancer cells while sparing normal tissue, preferential introduction of high Z material to tumour cells works as a method of radiation sensitization. Gold nanoparticles (GNPs) are very useful in this respect. It has been shown that the size, shape, and surface properties of GNPs affect their cellular uptake. Manipulation of the cell cycle to arrest cells at different stages offers a unique strategy to study the molecular and structural events as the cell cycle progresses. To optimize delivery of GNPs into tumour cells and enhance the effect of radiosensitization, nanoparticle (NP) uptake in synchronized populations of MDA-MB-231 breast cancer cells was investigated.

Populations of MDA-MB-231 cells were first synchronized in S-phase using double-thymidine block, and allowed to progress through cell cycle in synchronization. Synchronized cells were incubated with 5 nm GNPs, 15 nm GNPs, 46 nm GNPs and two formulations of lipid NP encapsulated 5 nm GNPs. Uptake of NPs was visualized using hyperspectral optical imaging and quantified with inductively coupled plasma mass spectrometry (ICP-MS). Following internalization of GNPs, cells were irradiated with 6 MV photon beams from a linear accelerator, and the survival fraction and induced deoxyribonucleic acid (DNA) damage were studied.

Cell cycle analysis after a double-thymidine block showed that the cell population was well synchronized. Uptake of NPs was 1.5-2 times higher in synchronized cell population compared to the control where cells were at different stages of the cell cycle. Clonogenic studies were used to evaluate the cell survival following radiation treatment. After a dose of 2 Gy, there was a decrease in cell survival fraction in synchronized cells treated with GNPs prior to radiation treatment compared to unsynchronized cells (control) indicating GNP-mediated dose-enhancement. The protein γ-H2AX, which is recruited to sites of DNA double strand breaks, was fluorescently labeled to evaluate damage due to the radiation treatment. Our results show more DNA double strand breaks in cells treated with GNPs prior to radiation. Interaction of ionization radiation with GNPs inside of cells produce secondary electrons. These secondary electrons can interact with water molecules and produce additional free radicals. These low energy electrons and free radicals interact with important cell structures and could cause cellular damage. Cell cycle synchronization has been shown to enhance GNP/PEG/RGD uptake in MDA-MB-231 cells resulting in greater cell radiosensitization and cellular damage. Cell synchronization is therefore an additional method available that can be employed to improve GNP uptake in cells.

Table of Contents

List of Tables

List of Figures

Symbols & Abbreviations

CDKs – Cyclin-dependent kinases
DLS – Dynamic Light Scattering
DNA – Deoxyribonucleic acid
DSB – Double strand break
EPR – Enhanced permeability and retention
FBS – Fetal bovine serum
FS – Field Size
GNP – Gold nanoparticle
ICP-MS – Inductively coupled plasma – Mass spectroscopy
LINAC – Linear Accelerator
LSPR – Local Surface Plasmon Resonance
MCL – Multicellular layers
MU – Monitor Unit (measure of machine output from a clinical accelerator for radiation therapy)
NP – Nanoparticle
PEG – Polyethylene Glycol
PBS - Phosphate Buffered Saline
RGD – Arginine-Glycine-Aspartic acid
RNA- Ribonucleic acid
ROS – Reactive Oxygen Species
RME – Receptor-mediated endocytosis
SF – Survival Fraction
TEM – Transmission electron microscopy
UV-VIS – Ultraviolet-Visible

Acknowledgments

I would like to thank my supervisor, Dr. Devika Chithrani, for her encouragement and guidance throughout my graduate studies.

I would also like to thank my fellow lab members Kyle Bromma and Aaron Bannister for their support.

I was also fortunate enough to have support from many individuals in different departments at University of Victoria. I would like to thank Dr. Perry Howard and Connor O'Sullivan for helping with flow cytometry, Dr. Jody Spence for nanoparticle quantification analysis, and Dr. Alexandre Brolo's group for their assistance with sample preparation for nanoparticle quantification studies.

I would like to extend my thanks to those at BC Cancer especially Dr. Wayne Beckham for assistance with radiation set up and training and the Deeley Research Centre where I was able to complete most of my experiments. Thanks to my committee members for taking time to assist and support me along the way.

This work would not be possible without the following granting agencies: Natural Sciences and Engineering Research Council of Canada (NSERC), Canada Foundation for Innovation (CFI), and British Columbia Knowledge Development Fund (BCKDF). I was supported by outstanding graduate entrance award, UVic fellowship, UVic graduate award, NSERC graduate scholarship, and our President's award during my graduate studies.

Chapter 1: Introduction

1.1 Radiation therapy in cancer treatment

Millions of people worldwide are diagnosed with cancer every year and almost half of Canadians will develop cancer in their lifetime. Cancer is an abnormal growth of cells caused by multiple changes in gene expression leading to deregulation of the balance of cell death and growth, ultimately evolving into a population of cells that can invade tissues and metastasize to other sites [1]. There are different treatment methods available for treating cancer patients and the health care team makes a decision on which to use based on the characteristics of the tumour cells. The most common methods are surgery, chemotherapy and radiation therapy. More than half of patients receiving treatment for cancer will receive radiotherapy as part of their treatment plan.

In radiotherapy, a high dose of ionizing radiation is delivered to the tumour site, which interacts and excites the atoms inside cells, causing damage to important structures ultimately killing the cell [2]. Radiotherapy is a good alternative to surgery for long-term control of many tumours in head and neck, lung, cervix, bladder, prostate, and skin. For breast cancers, a surgery is the primary treatment method often followed by post-operative radiotherapy delivered to the breast and regional lymph nodes [3]. The sources of radiation for treatment are gamma, x-ray photons, or charged particles, electrons, or protons [4].

External beam radiation therapy (EBRT) presents the challenge of delivering dose to tumour cells, while sparing normal tissue surrounding the target treatment volume. To help overcome this limitation novel approaches are constantly being developed or investigated to improve outcomes. Among other approaches, introduction of high atomic number materials as radiation dose enhancers into current radiation therapy protocol are being studied to improve the therapeutic effects [5]. For example, high atomic number material such as gold (Z=79) can be introduced to target material increasing the probability of ionization events leading to local enhanced deposition of energy causing more damage to tumour cells [6]. Gold nanoparticles (GNPs) are one of the materials

that are used extensively in cancer and nanomedicine research [7]. In this thesis, the therapeutic enhancement due to lipid nanoparticle encapsulated with smaller GNPs and individual gold nanoparticles of different sizes functionalized with peptide containing integrin binding domain Arginine-Glycine-Aspartate (RGD), and polyethylene glycol (PEG) are discussed.

1.1.1 Radiation therapy physics

X-rays have been used in clinic for treatment of cancer almost since their discovery in 1895 by Wilhelm Röntgen. Radiation therapy has become a recognized and widely used medical treatment method. The radiation used in these treatments is called ionizing radiation because it interacts with the material it is passing through and forms ions (charged particles) and deposits energy [8]. The energy deposited while passing through cells and tissue can kill the cancer cells. Radiation can be prescribed with the intent of curative treatment, but is also very effective in palliative care and relieving some of the symptoms a patient experiences due to the cancer.

The x-ray photons used in clinical radiation therapy external beam treatments are generated by a linear accelerator. Electrons are accelerated in the “wave guide” and then collide with a heavy metal target, producing high energy x-rays. Technological advances have facilitated the development of new imaging modalities, and delivery systems. For example, cancer clinics now have access to Intensity-Modulated Radiation Therapy (IMRT) where photon beam shape and intensity are varied throughout treatment delivery to precisely irradiate the tumour volume. Image-Guided Radiation Therapy (IGRT) can be used before treatment for localization of tumour volume or for imaging during treatment delivery to monitor tumour position real-time and improve precision and accuracy of radiation dose delivery. There are also different types of radiation used in radiation therapy treatment as discussed in the next section.

1.1.2 X-ray interactions with body

The human body is composed of different structures and organs, which are made of tissues that contain many millions of cells. Cells are made out of a few different types of building blocks. There are carbohydrates, proteins, lipids and nucleic acids; which together are categorized as biomolecules. These biomolecules are built out of atoms (carbon, hydrogen, oxygen etc.) and it is the charged particles with an atom that are important when discussing interactions of ionizing radiation with biological tissue.

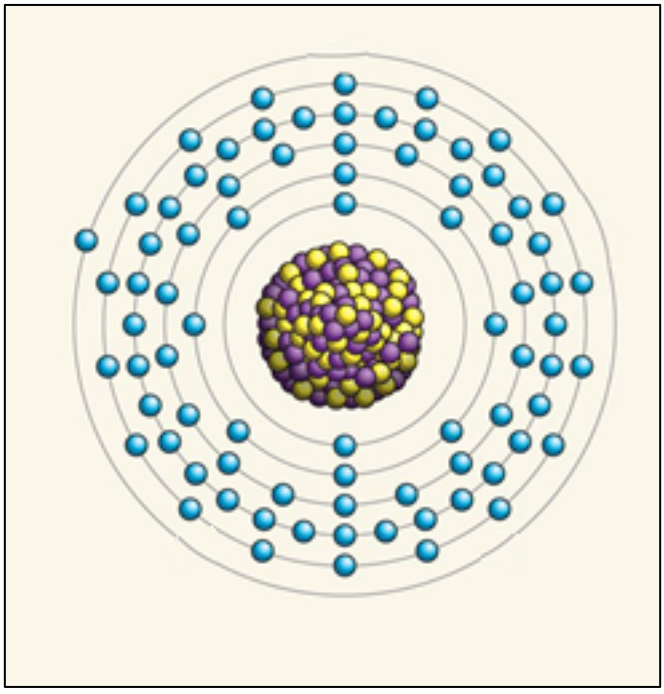

Figure 1. Atomic Structure. A cartoon representation of gold atom; a nucleus, composed of protons (purple) and neutrons (yellow) is orbited by electrons (blue), which occupy distinct shells. The components are not drawn to scale. Adapted from RightsLink: Springer Nature (Theoretical physics: sizing up atoms, Paul Indelicato, Alexander Karpov), 2013 [9].

An atom is made of a dense positively charged nucleus, surrounded by orbiting negatively charged electrons, as displayed in **Figure 1**. The nucleus is composed of Z protons and N neutrons. For a neutral overall charge the atom will have the same number of electrons as protons (Z). How the electrons fill the defined orbitals determines the stability or reactivity of an atom.

Electrons in the inner shells experience a greater attractive electrostatic force to the nucleus than an electron on an outer shell. The binding energy therefore depends on the shell considered as well as the atomic number Z, according to approximate Moseley rule:

$$W = 13.6\frac{(Z-b)^2}{n^2}$$

Where W is the binding energy of an electron (in eV), Z is the atomic number, n is the electron shell number and b is a constant used to correct for electrostatic screening effect due to there being electrons located between the nucleus and outer shell electrons. This number increases with outer shell electrons, giving less dependence on Z away from nucleus [10].

Photons have two types of interactions with absorbing media; interactions with nuclei and interactions with electrons. Interactions with nuclei can be described as photonuclear reactions and pair production. Photon interactions with electrons are categorized mainly as photoelectric effect and Compton scattering as illustrated in **Figure 2**.

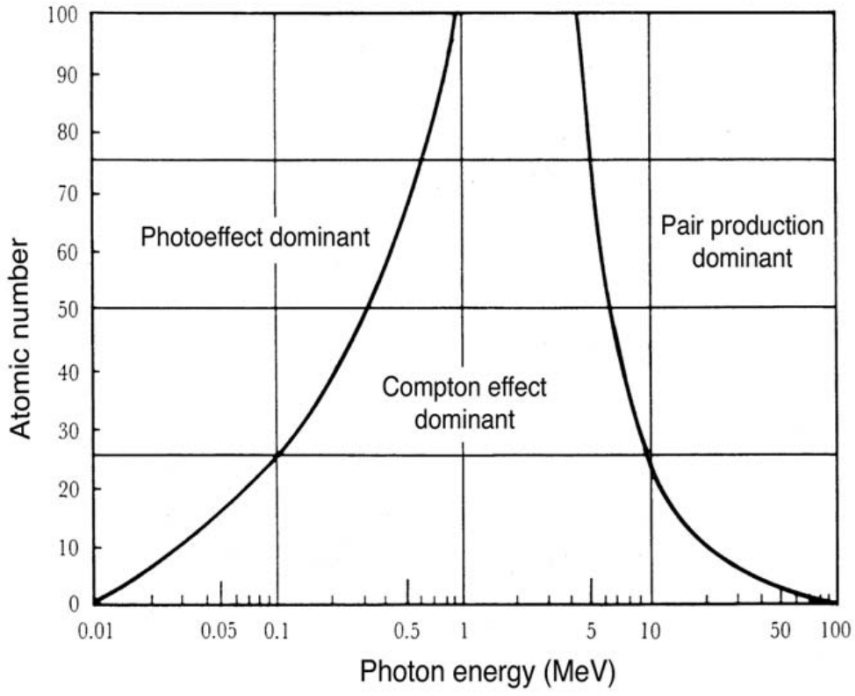

Figure 2. Regions of relative predominance of the three main forms of photon interaction with matter. Adapted from Podgorsak, E.B., Radiation Oncology Physics: A Handbook for Teachers and Students. 2005, Vienna: International Atomic Energy Agency.

An important parameter used for the characterization of x-ray or gamma ray penetration into absorbing media is the linear attenuation coefficient μ. This parameter depends on the energy of the photon beam and the atomic number of the absorber and gives a cross section (or probability of interaction). As previously stated photons can have different interactions with matter, so the probability of an interaction occurring is the sum of the cross sections of each of the interaction processes; photoelectric effect, pair production, incoherent scattering and Compton scattering.

The following equation is for the mass attenuation coefficient μ/ρ.

$$\frac{\mu}{\rho} = \frac{\tau}{\rho} + \frac{\sigma}{\rho} + \frac{\kappa}{\rho} + \frac{\sigma_R}{\rho}$$

where τ is the coefficient for photoelectric effect, κ represents pair production, σ and σ_R are Compton and incoherent scattering respectively.

Photoelectric Effect

In the photoelectric effect a photon is absorbed and ejects a tightly bound inner shell electron, leaving a vacancy in the orbital. The ejected electron is called a photoelectron. The energy of the photoelectron is the difference between the initial photon's energy and the binding energy of the electron. Following the ejection of an electron the atom with an orbital vacancy is in an excited state. To return to ground state an outer electron transits down to fill the vacancy. This will result in a release a photon with the binding energy difference between the two levels and the photon may travel away as a characteristic x-ray or cause an Auger electron to be ejected.

Compton and Rayleigh scattering

In a scattering process, the photon changes direction but is not completely absorbed. When the photon is scattered through only a small angle, without losing energy this is called Rayleigh scattering and does not have an effect on the energy deposited in the material. Compton scattering occurs when a photon interacts with a loosely bound electron in the atom. That electron is ejected, and the photon with reduced energy is scattered in another direction [4]. The Compton scattered photon may interact further, either by additional Compton scattering or by the photoelectric process. The probability

of Compton interaction is proportional to electron density, proportional to mass density, and less so on the atomic number Z.

Pair Production

Pair production is another absorption interaction. During this process, a photon is absorbed and an electron-positron pair is produced in the nuclear coulomb field. The threshold energy for pair production to occur is 1.022 MeV, the rest mass equivalent of pair of positively and negatively charged electrons. The probability of occurrence increases with increasing energy. Any excess energy is given to the electron-positron pair as kinetic energy. The electron is able to travel through media, losing energy through ionizing interactions. The positron will most probably undergo annihilation by reacting with an electron in the absorbing medium, creating two 0.511 MeV photons, that may interact with absorbing material.

X-rays photons of energy 6MV were used for experiments discussed in this thesis. At 6 MV photon energy, a common energy for clinical radiation therapy, the dominant interaction occurring is Compton scattering. For photons that have energy less than 150 keV, the photoelectric effect is dominant.

1.2 Biological considerations

Cancer is the abnormal growth of cells caused by multiple alterations in gene expression leading to deregulated balance of cell death and proliferation [1]. There are many different types of cells in the human body, from skin cells, to neurons, to liver or immune cells. However all eukaryotic cells do share some properties such as the cell membrane that controls import into and export out of the cell. Cellular components are constructed from food sources using internal systems for energy conversion (mitochondria), genetic material and gene expression encoding protein products that upon synthesis can assemble into larger structures [11].

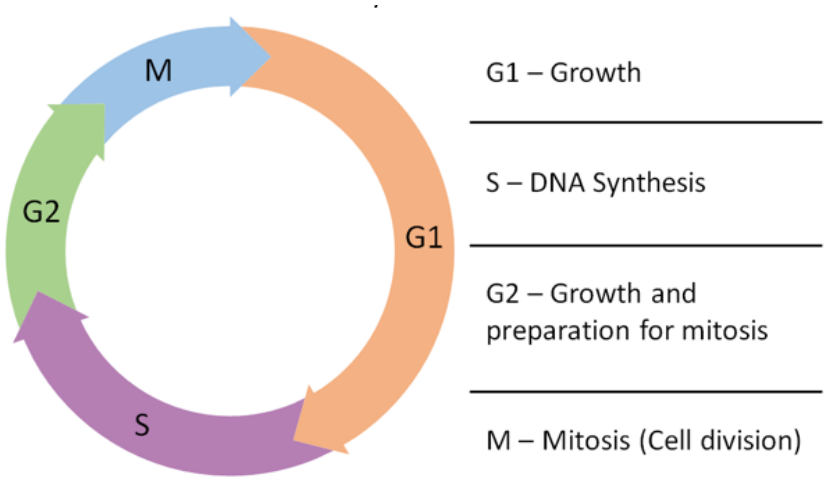

Figure 3. The phases of the cell Cycle. As a cell prepares for division it goes through three different phases: G1 is the gap between M and S phase, DNA replication occurs in S phase and G2 is when the cell prepares for mitosis.

The cell cycle is the process by which cells reproduce. In normal cells this is well regulated and requires the duplication of DNA and segregation of chromosomes into two daughter cells [12]. As illustrated in **Figure 3**, a eukaryotic cell cycle can be divided into four major phases; G1, S, G2, and mitosis. The genetic information is duplicated during S phase and the cell divides into two daughter cells during mitosis. S phase and mitosis are separated by Gap phases, G1 and G2. In eukaryotic cells G1 is where the most critical regulatory decisions are made.

Proteins are the triggers for progression through the cell cycle. The two different types of proteins are cyclins and cyclin-dependent kinases. All movement through the cell cycle is driven by cyclin-dependent kinases (CDKs) [2]. CDKs phosphorylate other proteins to initiate the processes required to continue through the cell cycle. For example, cyclinD-CDK4 is active in G1, and depending on extracellular signals, the cell makes the decision to commit to completing another cell division or to enter G0 (quiescence). To prepare for division the cell needs to grow; synthesize new ribonucleic acid (RNA), proteins, ribosomes, organelles and membrane.

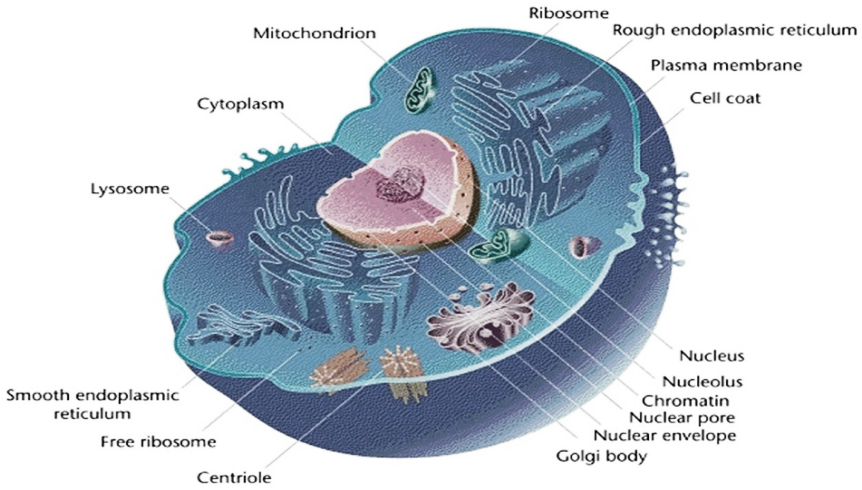

Figure 4. Eukaryotic Cell. A cartoon representation of the different organelles in a eukaryotic cell. Adapted from Mediran [CC BY-SA 3.0], via biologydictionary.net/eukaryotic-cell

A cross-section of a eukaryotic cell is explained schematically in **Figure 4**. The most important parts of the cell are labelled. For example, the plasma membrane separates the cell from its environment. It is formed by a phospholipid bilayer. The key property is that the lipids are amphipathic; they contain a hydrophilic head and have hydrophobic tails. This causes water and other polar molecules to stay on one side of the membrane. This amphipathic nature also drives self-assembly of membranes, with the lipids merging with hydrophobic tails together and away from the polar solution [13]. The cell membrane's role is regulating the internal environment and creating and maintaining concentration gradients. Cell must be able to import sources of energy and precursors for cellular components to be formed e.g. fatty acids are used to build lipids, amino acids form proteins and nucleotides make deoxyribonucleic acid (DNA) and RNA [11].

There are a variety of proteins included in the cell membrane categorized as integral and peripheral proteins. Integral proteins span the entire thickness of the membrane and are often involved in communication between the intracellular and extracellular compartments. Peripheral proteins are attached to only one leaflet of the plasma membrane and are usually involved with cellular skeleton. The area contained by the plasma membrane is called the cytoplasm. This is mostly water, containing solutes

such as calcium, sodium and potassium ions. Within the cytoplasm are also other important organelles.

One of the most important components of the cell is mitochondria which is colloquially called the powerhouse of the cell. These have two layers of phospholipids forming the outer membrane and inner membrane, which has many folds. This inner membrane in the mitochondria is where the electron transport system occurs which produces energy for the cell.

Nucleus of the cell can be considered as the brain of the cell. This houses the cell's genetic material (mitochondria have own genetic material). Double helix DNA strands form the chromosomes in the nucleus. Humans have 23 pairs of chromosomes that contain the genetic information unique to that person. DNA guides the function of cellular machinery through the processes of transcription and translation- process of forming RNA and subsequently proteins. Cellular DNA is made up of two complementary strands of bases linked by hydrogen bonds and connected by a sugar-phosphate backbone forming a double helix. Because DNA is such an important molecule for the cell and there are only two copies, accurate replication and quick repair of damage is necessary.

There are different types of damage to DNA that can occur. Single-strand breaks are the result of a break in one strand of the sugar phosphate backbone, these are readily repaired using the opposite strand as a template [14]. Damage to both intertwined strands of a DNA duplex is called a "double-strand break" (DSB) and can cause permanent damage to DNA that is lethal to the cell. For this reason, when assessing cell survival DSBs are most significant. When DNA is damaged or DNA-replication errors occur, monitoring proteins like tumour suppressor p53 sense the damage and halt the cell cycle until the damage can be repaired or apoptosis is initiated [12].

MDA-MB-231 tumour cells were used for the experiments discussed in this thesis. It is an epithelial human breast cancer cell line that was established from pleural effusion of a 51-year-old woman with metastatic mammary adenocarcinoma. It is an adherent cell line and can grow in tissue culture dishes to carry out experiments for testing different treatment options *in vitro* before testing them in animal models. Previous studies have been conducted using GNPs and MDA-MB-231 cells. Those studies showed

that uptake of GNPs by cancer cells caused significant radiosensitization [15]. Each type of cancer will have unique characteristics and respond differently to treatment. Experimental results were acquired using the MDA-MB-231 cell line and give insight into how further studies could be optimized that would lead to development of clinical treatment implementing gold nanoparticles as radiosensitizers.

1.3 Radiobiology

Radiation dose is measured in units of Gray (Gy). This is the standard unit of absorbed dose in Joules per kilogram, 1 Gy = 1 J/kg. Each Gy of ionizing radiation causes 10^5 ionizations, >5000x base damage, 1000 single-strand breaks and 40 double-strand breaks per cell [2]. This would however only kill about 30 percent of the cell population, because the cell is very efficient at DNA repair [2]. Double strand breaks are most difficult to repair and are the primary mechanism of damage of ionizing radiation. In radiobiology cell death is defined as loss of reproductive capability. A cell with severe DNA damage may continue to grow and divide for a short time before it is no longer able to divide. This is why cell survival is typically measured after enough time has passed that the survival fraction truly represents undamaged and proliferating cells.

The principal damaging effect of ionizing radiation comes from the ability of the high-energy photons to excite and ionize molecules within the cell. Most damage is caused by the electrons ejected from excited atoms. They have kinetic energy and as the electron travels it will collide with molecules, progressively slowing down. Near the end of the electron's track, ionization events are more frequent, causing a cluster of ionizations that are comparable to the size of the diameter of the DNA double helix (2.3 nm) [2]. When the density of ionization along a particles track is higher there may be more lethal lesions or high-LET (linear energy transfer) radiation damage is less likely to be repaired correctly.

Ionizing radiation deposits energy randomly, and will effect most of the molecules in the cell. However, there are multiple copies of most molecules, which undergo rapid turnover (e.g. mRNA, proteins). DNA on the other hand only has two

copies, has limited turnover, is the largest molecule and is central to cellular function [2]. The creation of double-strand breaks (DSBs) represents the principal lesion that, if not adequately repaired, can lead to cell death. There are different complex damage response mechanisms to protect the cell, where the checkpoints in the cell cycle become very important as the cell will continue forward through the cell cycle and undergo division only when the appropriate signalling molecules are present.

Two principal recombination DNA repair pathways are homologous recombination (HR) and nonhomologous end-joining (NHEJ). In HR an undamaged sister chromatid sequence is used as a template to repair the DNA with DSBs in it, typically in S or G2 phase of cell cycle [16]. Nonhomologous re-joining of two double-stranded DNA ends, which may occur in all cell-cycle phases, does not require an undamaged partner and does not rely on extensive homologies between the recombining ends.

The main goal of radiation therapy (RT) is to take away the cell's ability to multiply, thus killing the cell. If damage to a cell is not adequately repaired, RT could induce apoptosis (programmed cell death), mitotic catastrophe, necrosis or autophagy. Apoptosis is the cell's programmed cell death mechanism. It results in rapid destruction of the cell, initiated by the cell itself in response to damage or stress. Mitotic catastrophe is cell death that results from aberrant mitosis; this is thought to occur when cells enter mitosis with damaged DNA. Necrosis occurs under extremely unfavourable conditions such that normal physiological function is not possible, it is considered to be 'accidental cell death'. Autophagy is a term used to describe a process where the cell digests parts of its own cytoplasm to generate small macromolecules and energy [2]. The form of cell death that is occurring in a tumour in response to radiation may influence the rate at which cells die.

1.4 Radiosensitization

Radiotherapy is one of the most widely used treatment approaches; X-ray photons have been used to treat cancer since the end of the 19th century (shortly after the discovery of x-rays by Wilhelm Röntgen in 1895). Based on statistics, 7 times as many

patients have been cured with radiotherapy than chemotherapy [2]. Therefore, improvements in method using sensitizing agents could have a very big impact in the treatment of cancer in the near future.

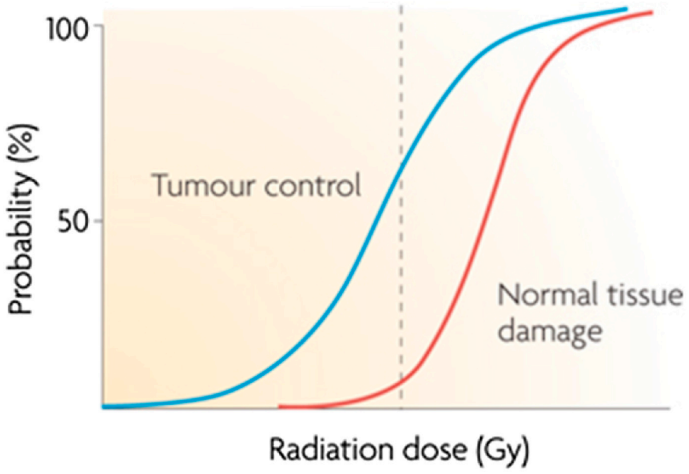

Figure 5. The therapeutic ratio. Probability of tumour control (blue) has sigmoid-shaped response as radiation dose increases. The probability of normal tissue damage/complication (red) is also shown. The dashed line indicates 60% tumour control and 5% normal tissue complication. Reprinted from [17] with permission from Springer Nature.

Curative treatment goal is 100% tumour control. As illustrated in **Figure 5**, it is clear and logical that as radiation dose increases tumour response also increases. Tumours however are not perfectly shaped but irregular masses seated within the patient surrounded by normal healthy tissue. Modern radiotherapy techniques such as IMRT and VMAT (volumetric modulated arc therapy) have made great advances in delivering dose to tumour cells while sparing normal tissue. In techniques such as these, the shape of the beam is modified by moving leafs in the collimator of the linear accelerator, intensity of the beam is modified and the gantry is rotated around the patient. The continually improving technology makes it possible to precisely sculpt the dose distribution to the treatment volume while sparing surrounding normal tissue. However dose to normal

tissue cannot be avoided completely and normal tissue will also receive dose during radiation treatment as shown in **Figure 5**. In the clinic, physicians set the upper limit of tolerance for normal tissue toxicity and the factors considered includes not only negative side effects from a medical perspective but also the patient's quality of life. This limitation in the radiation dose puts a limit of achievable tumour response. One method to improve the therapeutic index without causing much toxicity to normal cells is the introduction of radiosensitizing agents. Specifically targeted radiosensitizing agents would increase tumour response; this would be seen as a movement to the left of the tumour control curve in **Figure 5**. Damage to normal tissue will likely also increase, also shifting the curve, but if the curves move further apart the therapeutic index has increased. This means that greater tumour control can be achieved, while minimizing normal tissue damage.

1.4.1 Gold nanoparticle as radiosensitizer

The use of high atomic number (Z) material to enhance radiation dose has been studied for more than 50 years. The interest in using high-Z material stems from the production of secondary electrons scattering from high-Z material. The atomic number of tissue is approximately Z~7.5, so materials with a higher atomic number used in the past include Iodine (Z=53), bulk gold (Z=79) and micrometer sized gold particles. For example, Matsudaira *et al.* showed that intratumoural injection of iodine and 200 kVp X-ray radiation suppressed the tumour growth by 80% [18]. Another study showed that brain tumours in mice irradiated with iodine contrast agents (15 Gy, 120 kVp X-rays) produced a 30% enhancement in radiation dose [19]. Nath *et al.* demonstrated that incorporating iodine into cellular DNA using iododeoxyuridine enhanced radiosensitivity by a factor of three [20]. Use of gold as a radiation dose enhancer has gained much interest in the recent past as discussed in the next section.

In addition to having a great difference between mass attenuation between gold and soft tissue, gold has been shown to be biocompatible, easy and economical to manufacture in many different shapes and sizes [21]. Research has been done investigating gold nanoparticles as radiosensitizers, since these particles can be delivered

to tumour cells within a patient. Nanoparticles are microscopic particles 1-100 nm in size, which provides good penetration ability through tissue. Radiation dose enhancement in kilovoltage (kVp) energy range is mainly due to the increased probability of photoelectric effect [7].

Using 1.9 nm GNPs and 250 kVp X-rays Hainfield *et al*. delivered 30 Gy dose to subcutaneous tumours in mice. This is one of the pioneering studies in GNP-mediated radiation dose enhancement. The outcome was significant since the mice that were treated with GNPs and radiation had tumours that were no longer visible or shrinking and had 86% long-term survival versus 20% with x-rays alone and 0% with gold alone [22].

1.4.2 Radiosensitization mechanisms of gold nanoparticles

Exposure of biological systems to radiation activates a series of mechanisms, which can be divided into physical, chemical and biological. These mechanisms differ in the time for effects to occur. Ionizing radiation interacts with biomolecules, causing ionization and excitation of atoms, as well as formation of free radicals [23]. The physical mechanism of GNP radiosensitization occurs within the first nanoseconds of exposure and is based on the difference in energy absorbance between gold and soft tissue. This enables dose enhancement in the presence of gold. The photoelectric effect is the predominant mode of interaction for 10 to 500 keV photons. As shown in **Figure 6** the mass energy coefficient of gold is 100-150 times greater than that of soft tissue in keV energy range [24].

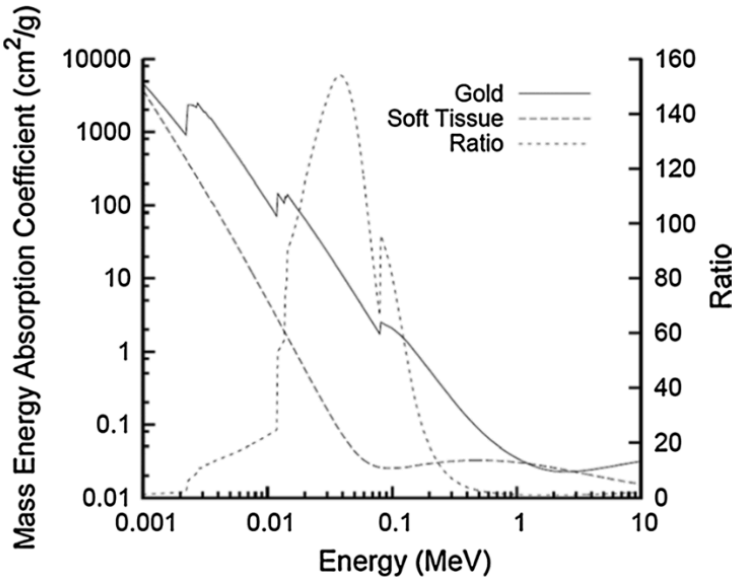

Figure 6. Photon mass energy absorption coefficients of soft tissue and gold. The ratio of mass energy absorption coefficients is shown as a function of photon energy. Reprinted from [24] with Creative Commons licence: https://creativecommons.org/licenses/by/4.0/legalcode.

Interactions of photons with gold atoms are illustrated in **Figure 7**. For example, photons of energy above 500 keV Compton scattering is observed, where an incident photon is scattered off a weakly bound electron [25]. In this process a small amount of energy is transferred from the photon to the electron, and the electron is emitted from the atom [23]. The scattered photon has lost some energy, but will continue along its new path. In the photoelectric effect, the incident photon is fully absorbed and electrons are preferentially ejected from inner atomic orbital. The vacancies created in a K, L or M inner orbital are filled by an outer-shell electron. This process would lead to release of lower energy photons and a cascade of secondary electrons called Auger electrons.

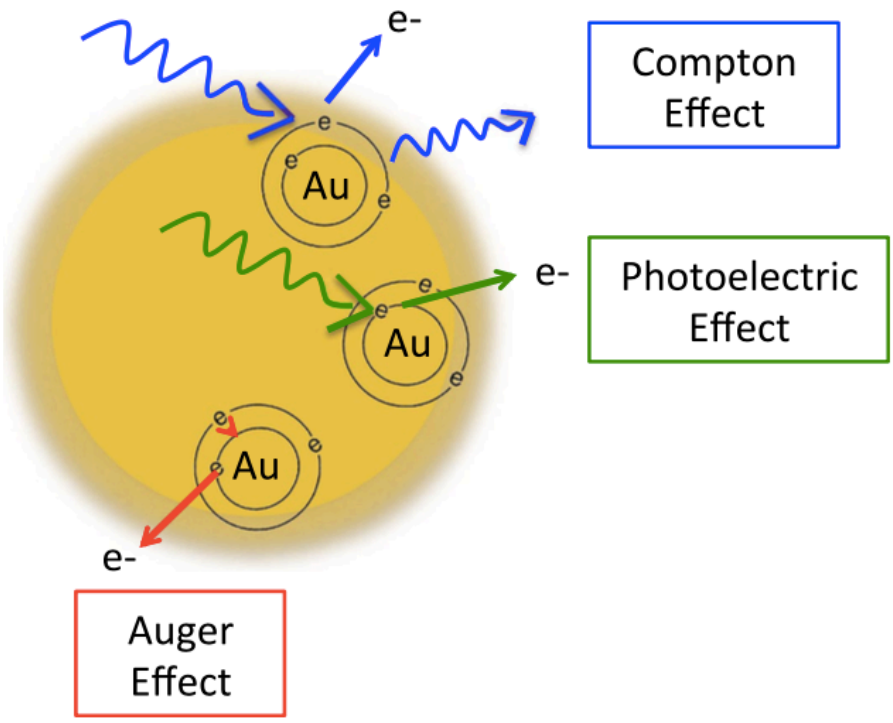

Figure 7. Illustration of the ionization interactions of a photon and GNP. Shown are the photoelectric effect (green), Compton effect (blue) and Auger effect (red). Reprinted from [24] with Creative Commons licence: https://creativecommons.org/licenses/by/4.0/legalcode.

The range of electrons released from GNPs is short, only a few micrometers. This causes highly localized ionizing events and to achieve any enhancement from GNPs in radiation therapy, GNPs must be delivered and internalized specifically by tumour cells.

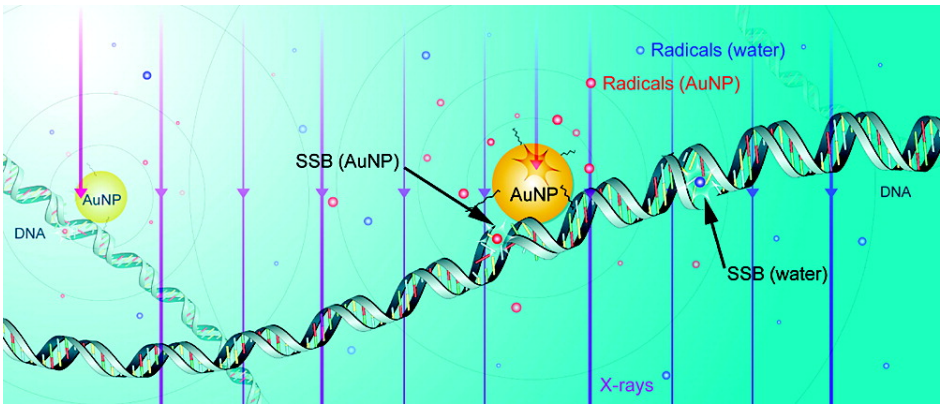

Figure 8. Schematic showing chemical mechanism of GNP radiosensitization. Reprinted with permission from [26]. Copyright (2007) American Chemical Society.

The chemical mechanism of GNP radiosensitization occurs through radiochemical sensitization of DNA by increasing catalytic surface activity and radical generation by GNP surface [27]. For the mechanism of GNPs acting as a catalyst, studies have shown this is possible due to the electronically active surface of a GNP. Gold nanoparticles can catalyze chemical reactions and exhibit electron transfer from surface-bound donor groups to O_2 molecules, generating free radicals as illustrated in **Figure 8** [27]. For this mechanism, GNPs would need to be localized in the nucleus and have access to DNA. This seems more evident in small GNPs (< 5 nm in diameter) where surface to volume ratio is greater [28].

The biological mechanisms of cellular response to GNPs results in production of reactive oxygen species (ROS), oxidative stress, and cell cycle effects [24]. Oxidative stress causes damage to cell membrane, DNA and proteins [29]. Mitochondria seem to play a role and the data indicates loss of function due to high intracellular ROS levels. This is supported by experimental findings that use of 1.4-nm triphenyl monosulfonate (TPPMS)-coated GNPs resulted in a loss of mitochondrial potential through elevated oxidative stress causing necrotic cell death [30]. There have been studies suggesting that GNPs may cause cell cycle disruptions and induce apoptosis. Radiosensitivity varies throughout the cell cycle with S phase being where a cell is most radioresistant and G2/M phase being most sensitive [31]. This could also depend on cell type, and expression of cyclin kinases and NP characteristics such as coating and size. For example, use of 1.9

nm GNPs in DU-145 prostate cancer cells and MDA-MB-231 breast cancer cells resulted in an increase in sub-G1 population in DU-145 population but not in MDA-MB-231 [32].

1.5 Uptake dependence on GNP size, shape and functionalization

In order to have any dose enhancement, GNPs need to accumulate in tumour cells. There is natural accumulation of NPs in tumours due to leaky vasculature of tumours and what is called the enhanced permeability retention effect (EPR) [33]. Cancer cells are rapidly dividing cells, and as the tumour is growing production of blood vessels is being stimulated to provide blood flow to the growing mass. The vasculature surrounding the tumour is usually abnormal, with the integrity of the vessel walls compromised particles on the nano-scale easily escape the vessels and accumulate in the tumour environment [33]. However the size, shape and functionalization of GNPs can also be optimized to maximize uptake by tumour cells as illustrated in **Figure 9**. Studies of different sized colloidal GNPs showed that the maximum uptake occurred when NPs have 50 nm diameter as shown in **Figure 9A**. GNPs of this size are able to more efficiently enter cells via receptor-mediated endocytosis [34].

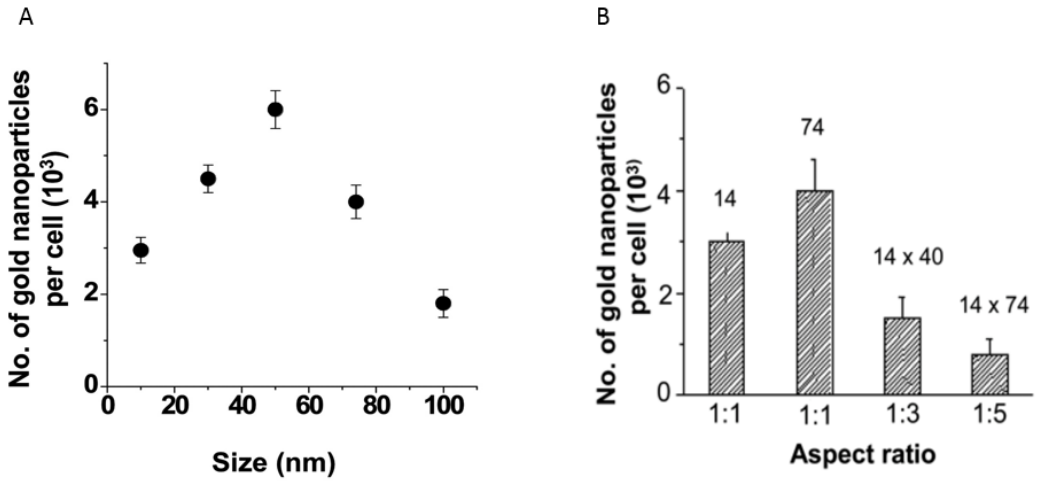

Figure 9. Effect of size and shape on cellular uptake of gold nanoparticles. A) Dependence of gold nanoparticle cellular uptake as a funtion of their diameter. B) Comparison of uptake of rod-shaped nanoparticles (aspect ratios 1:3 and 1:5) and spherical nanoparticles (1:1). Reprinted with permission from [34] Copyright 2006 American Chemical Society.

Chithrani *et al.* [34] also investigated the effect of shape on GNP internalization by HeLa cells (a cervical cancer cell line) (see **Figure 9B**) . They found that the uptake of rod-shaped NPs were lower than their spherical counter parts. They argued that it could be due to the difference in surface chemistry. Non-specific adsorption of serum proteins like α- or β-globulin onto spherical GNPs was greater than the rod-shaped NPs. Many serum proteins like α- or β-globulin are known to be taken in by cells along with NPs [34].

To have an efficient NP system, prolonged *in vivo* residency time and preferential localization in tumour environments is necessary [35]. Surface modifications of GNPs are done to protect the particle from the environment and to target the particle to a specific cell or tissue type. It has previously been shown in many studies that adding polyethylene glycol (PEG) to the surface of NPs increases blood circulation time [36, 37]. This is important because the NPs need to be present long enough for the process of accumulation within a tumour through its leaky vasculature. PEG functionalized NPs have the capacity to evade the immune system and remain in the blood undetected by macrophages [35]. In addition to PEG molecules, a peptide containing Arginine-glycine-aspartic acid (RGD) sequence can be added to NP surface to improve tumour cell targeting as shown in **Figure 10**. The peptide containing RGD sequence can recognize the integrin αvβ3 that is highly expressed by several solid tumours [35, 38].

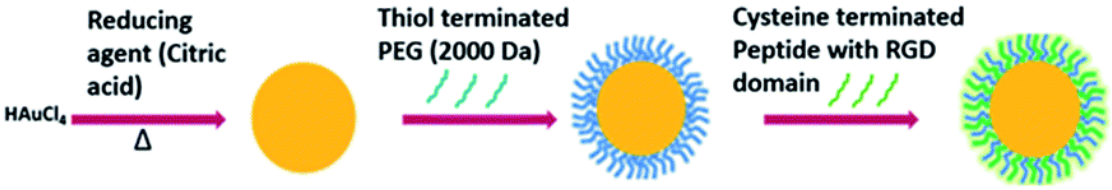

Figure 10. Functionalization of GNPs. Nanoparticles were first functionalized with PEG followed by a peptide containing RGD domain. RSC advances by RSC Publishing. Reproduced with permission of RSC Publishing in the format Thesis/Dissertation via Copyright Clearance Center [35].

The GNPs used in this thesis are 15 nm and 46 nm in diameter, functionalized with PEG and RGD peptides. This decision was made based on previous results stating that 50 nm GNPs have highest uptake at single cell level *in vitro*. However, the smaller 15 nm GNPs are able to penetrate through the extracellular matrix and are therefore more accessible to tumour cells *in vivo*, therefore both systems are investigated.

GNPs enter cell mostly via receptor-mediated endocytosis (RME) as explained in **Figure 11**. Receptor-mediated endocytosis of NPs occurs through interactions between the proteins on the surface of the nanoparticle and receptors on the cell membrane. Cell surface receptors binds to molecules on surface of NPs causing membrane wrapping of the NP with a corresponding increase in elastic energy [39]. The receptor-ligand binding immobilizes receptors causing configurational entropy to be reduced. More receptors diffuse to the wrapping site, driven by the local reduction in free energy, allowing the membrane to wrap completely around the particle [40].

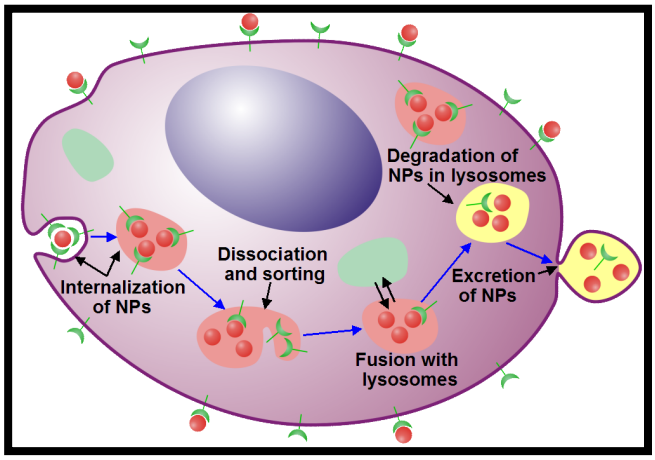

Figure 11. Uptake of GNP by receptor-mediated endocytosis. Schematic illustrating pathway of citrate-capped GNP uptake into the cell. Once GNPs are attached to the receptors on the surface of the cell, membrane wrapping occurs followed by budding into the cell, forming a vesicle. The internalized GNPs are sorted inside the vesicle and eventually fuse with lysosomes. GNPs are then excreted out of the cell. This is called the endo-lyso pathway [38][35].

Receptor mediated endocytosis is therefore an energy dependent process. The path of the NPs within the cell is explained in Figure 11. For example, once GNPs are bound to the receptors on the surface of the cell, membrane wrapping occurs followed by trapping NPs in endosomal vesicles. The internalized GNPs are sorted inside the vesicle and eventually fuse with lysosomes. GNPs are then excreted out of the cell. This is called the endo-lyso pathway.

1.6 Lipid nanoparticles

The design and development of new nanoparticle delivery systems is motivated by the goal to create new materials and devices with superior properties, functions, efficiencies and safety [41]. Lipid nanoparticles (LNPs) are composed of lipid materials that are solid at room and body temperature, such as triglycerides and fatty acids [42]. Lipid nanoparticles are being investigated as drug carriers, it is estimated one third of anti-cancer drugs are hydrophobic, but are also potentially useful in overcoming toxicity presented by small metallic nanoparticles. The vesicle carrying entrapped GNPs protects and preserves the native characteristics of GNPs but is also very exciting in that it provides a framework in which multiple therapeutic methods can be combined as illustrated in **Figure 12** [41].

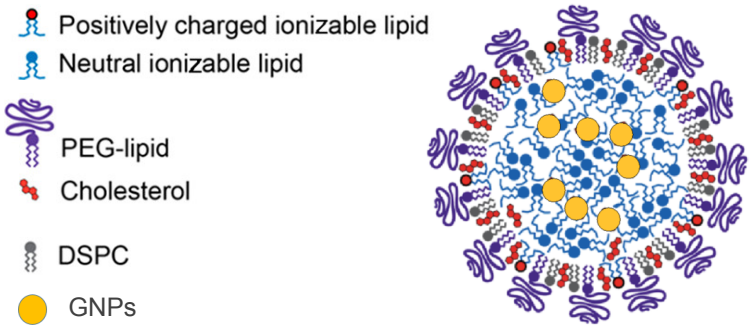

Figure 12. Gold nanoparticle incorporated lipid nanoparticle structure. LNP systems are formed from lipid mixtures (cationic lipid, distearoylphosphatidylcholine, cholesterol and PEG-lipid).

1.7 Scope of thesis

The focus of this research was to understand whether there is a difference in cellular uptake and radiation dose enhancement in a synchronized cell population *vs*. a control cell population where phase of each cell can vary. Three different nanoparticle complexes were tested:

a) Small 5 nm gold nanoparticles incorporated in lipid nanoparticle systems.
b) Gold nanoparticles of diameter 15 nm functionalized with PEG and a peptide containing a RGD domain.
c) Gold nanoparticles of diameter 46 nm functionalized with PEG and a peptide containing a RGD domain.

A triple negative breast cancer cell line, MDA-MB-231 was used to conduct all of the experiments. This cell line is an aggressive line of adherent breast cancer cells, and was chosen because searching for improvement in radiation dose delivered to more aggressive tumour types is very worthwhile and finding improvement here may carry over to other cell types. Thymidine blocking was used to synchronize cells in S phase. Tumour cells were treated with NP complexes before administering a 2 Gy dose of 6MV photon radiation. Both clonogenic and DNA double stand breaks assays were used to determine the effect of radiation treatment on cell damage and survival.

Chapter 2: Methods

2.1 Synthesis of gold nanoparticles

Gold nanoparticles were synthesized using the citrate reduction method [43]. First, 300 µl of 1 % chloroauric acid ($HAuCl_4 \cdot 3H_2O$) (Sigma-Aldrich) was added to 30 ml of double–distilled water and brought to boil on a hot plate while stirring. The amount of the reducing agent added varied depending on the size of the NPs.

For example, through optimization studies performed it was determined that the addition of 1 ml and 300 µl of 1 % sodium citrate tribasic dehydrate (HOC $(COONa)(CH_2COONa)_2 \cdot 2H_2O$) (Sigma-Aldrich) synthesized 15 nm and 46 nm GNPs, respectively. After the color of the solution changed from dark blue to bright red, the solution was left to boil for another ten minutes while being stirred. Finally, the GNP solution was brought to room temperature while being stirred.

2.2 Functionalization of gold nanoparticles

Polyethylene glycol (PEG) is added as a surface coating to GNPs to prolong blood circulation *in vivo* [35]. In order to evade uptake by macrophage cells of the immune system, a minimum density of 1 PEG per nm^2 is required on GNP surface [44]. Absence of nonspecific protein adsorption in blood results in a prolonged blood circulation, which increases the chances for GNPs to accumulate within the tumour using its leaky vasculature. PEG that was 2000 Da molecular weight was used to coat the GNP surface because it is closer to the molecular weight of the other molecule coating the surface, the peptide used for improved uptake of NPs RGD (1760 Da). A 0.01mg/ml PEG solution was prepared with thiol-terminated PEG methyl ether. The PEG solution was added to GNP solution to achieve density of 1 PEG per nm^2. For 15 nm and 46 nm GNP, 706 and 6648 PEG were added per NP, respectively [37].

Polyethylene glycol would minimize uptake at cellular level, therefore a peptide containing integrin-binding domain, RGD, was added in combination with PEG. A solution with peptide sequence CKKKKKKGGRGDMFG was added to the gold solution. The RGD working solution had a concentration of 0.0125mg/ml and the molecular weight was known from the manufacturer's data sheet to be 1669.5g/mol, giving a concentration of $4.5x10^{12}$ RGD peptides per ml. For 15 nm and 46 nm GNPs, 361 and 3307 RGD peptides were added per NP, respectively [37].

2.3 Lipid nanoparticle synthesis

Our lipid nanoparticle systems were synthesized by Dr. Jayesh Kulkarni at the University of British Columbia (UBC). GNPs of diameter 5nm were purchased from Ted Pella, Inc. (Redding, CA); these GNPs were used alone as well as entrapped in lipid nanoparticles to allow comparison of improvement in uptake. 5 nm GNPs were entrapped in lipid nanoparticles (LNPs) using microfluidic mixing method. Two formulations (A and B) were prepared, the difference between them being the gold-to-lipid ratio. Lipids (composition is DLin-MC3-DMA/DSPC/Cholesterol/PEG-lipid (50/10/39/1 mol%)) were first dissolved in ethanol at 20 nM concentration. Gold nanoparticles were suspended in 25 mM sodium acetate buffer (pH4) to a ratio of $2.2x10^{13}$ GNP/μmol lipid for formulation A and $8.8x10^{13}$ GNP/μmol lipid for formulation B. The organic phase and aqueous phase were mixed through a T-junction mixer (PEEK 0712) at a flow rate ratio of 1:3 v/v (or 5mL/min ethanol and 15 mL/min aqueous). The resulting suspension was then dialyzed into phosphate buffered saline (PBS) and concentrated ~4-fold following dialysis. PBS is a common buffer used in biological research, the osmolarity and ion concentration (sodium chloride, and potassium phosphate) match those of the human body, while also helping to maintain the pH of the solution. This process forms (LNPs) that no longer have a typical bilayer structure, but rather an electron dense core, a significant fraction of the lipids are contained within the particle's core. The surface of the LNPs was functionalized with PEG at UBC as well.

2.4 Characterization of gold nanoparticles

2.4.1 Ultraviolet-visible spectroscopy

Once GNP complexes were synthesized, different measurements were performed to determine characteristics of the nanoparticles such as size, charge and functionalization. One of property measured was the absorbance of ultraviolet-visible light to determine the size and concentration of GNPs in solution. An Ultraviolet-Visible (UV-Vis) spectrometer was used to measure the absorbance of ultraviolet or visible light by a sample by performing a scan over a range in the electromagnetic spectrum; UV region 190-400 nm, and visible 400-800 nm. The schematic diagram highlighting the important components of the UV spectrometer is shown in **Figure 13**. Gold nanoparticles exhibit the optical feature known as localized surface plasmon resonance (LSPR); the collective oscillation of electrons in the conduction band of GNPs resonate with a specific wavelength of incident light, specific to the GNPs size. UV-Vis measurements were performed using Perkin Elmer LAMBDA 365 with wavelength range of 400 to 600 nm and a resolution of 0.05 nm. 2ml of GNP sample was measured in a 1cm path length cuvette. The light source (deuterium and tungsten) provides visible and near ultraviolet radiation covering 200-800 nm. Output is focused on a diffraction grating that splits incoming light into colours of different wavelengths. The sample of GNPs was in a cuvette, with a cuvette of deionized water serving as reference. For each wavelength the intensity of light passing through the sample is measured (I) as well as reference cell (I_o). If I is less than I_o, the sample as absorbed some light.

Absorbance (A) is related to I and I_o according to the following equation:

$$A = \log_{10} \frac{I_o}{I}$$

The detector converts the incoming light into current, higher current indicates higher intensity.

According to the Beer-Lambert Law, the absorbance is proportional to concentration of the substance in solution. Beer-Lambert Law is expressed as follows:

$$A = \varepsilon c l$$

A = absorbance

l = optical path length (dimension of cuvette) =1cm

c = concentration of solution (mol dm^{-3})

ε = molar extinction ($dm^3mol^{-1}cm^{-1}$)

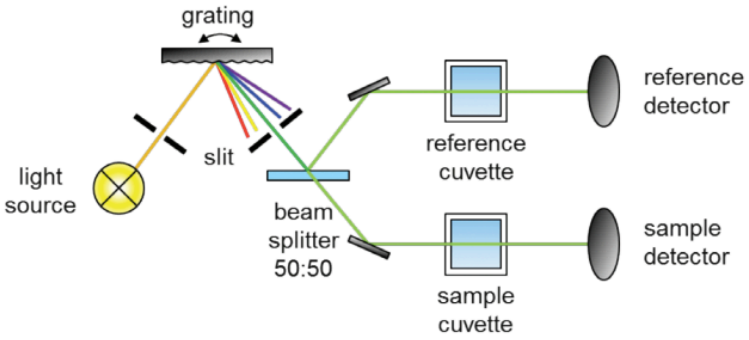

Figure 13. Schematic of Ultraviolet Visible spectrometer.

The diameter of GNPs was determined using Mie theory, which is a solution of Maxwell's equations involving the absorption and scattering of electromagnetic waves by spherical particles [45]. Here the wavelength of surface plasmon resonance peak, or ratio of the absorbance of GNPs at the surface plasma resonance peak to absorbance at 450 nm is related diameter of GNPs and concentration calculated using the extinction coefficients that have been previously experimentally validated [45]. Molar extinction coefficient (ε) at λ=450 nm was taken from a look up table for each size of GNP, where it was calculated from the fit to the theoretical extinction efficiencies for GNPs in water with diameter ranging from 2 to 100 nm. The wavelength 450 nm was used because there is a better agreement in experimental results and theory if the absorbance ratios are determined in a wavelength region below 600 nm [45]. An exponential function can be used to fit both experimental and theoretical peak wavelength position:

$$\lambda_{spr} = \lambda_o + L_1 e^{(L_2 d)}$$

With fit parameters determined from theoretical values (λ_o=515; L_1=6.53; L_2=0.0216) [45].

For 15 nm GNPs, ε_{450} is 2.18 x 10^8 $M^{-1}cm^{-1}$ while it is it was 7.65 x 10^9 $M^{-1}cm^{-1}$ for 46 nm GNPs [45]. The concentration of GNPs in solution was determined using the following equation:

$$C = \frac{A_{450}}{\varepsilon_{450}}$$

2.4.2 Dynamic light scattering (DLS)

The hydrodynamic diameter measured using DLS is the diameter of a hypothetical hard sphere that diffuses with the same speed as the particle under examination. This is a way to get accurate particle size measurements and confirm size of GNPs measured with UV-Vis.

Macromolecules in solution undergo random Brownian motion. Particles are constantly moving and their motion is uncorrelated to that of other particles. Random motion can be modeled by Stokes-Einstein equation, which relates diffusion coefficient measured by Dynamic Light Scattering (DLS) to particle size.

$D_h = \frac{k_B T}{3\pi\eta D_t}$;

Where D_h - hydrodynamic diameter

D_t - translational diffusion coefficient

k_B - Boltzmann's constant

T - Thermodynamic temperature

H - dynamic viscosity

Light scatters off of the randomly moving particles, and introduces randomness to the phase of scattered light. Time-dependent fluctuations in the intensity of the scattered light are measured by a fast photon counter. The fluctuations are directly related to the rate of diffusion of the molecule through the solvent, which is related in turn to the particles' hydrodynamic diameter. Smaller particles move faster than larger ones. Hydrodynamic diameter is the diameter of a sphere that sphere that diffuses the way the particle does. Measurements were taken using Anton Paar Litesizer™ 500 and samples in 1 cm disposable cuvettes. The light source is a laser light of wavelength 658 nm. The

measured data is the correlation curve; fitted to an exponential function and the results from DLS give an average size of particles, as well as the size distribution.

2.4.3 Zeta potential

The zeta potential is the measure of the electric charge on the nanoparticle surface. This gives us information about the particles' stability; a larger zeta potential means greater stability due to larger electric repulsion between particles. Zeta potential was measured by electrophoretic light scattering (ELS), which measures the speed of particles in an electric field. Measurements were taken using Anton Paar Litesizer^{TM} 500. Gold nanoparticle samples were loaded into clean Omega cuvettes and readings were taken at room temperature.

2.4.5 Dark-field and hyperspectral imaging

A Hyperspectral Imaging System was used in conjunction with the dark-field microscope to obtain reflectance spectra from each pixel in the dark-field image. The CitoViva technology used allows for visualization of GNPs in cells without requirement of any additional labeling [46-48]. Spectral Angle Mapping can be performed to conduct a pixel-by-pixel matching of any spectra obtained by the system. This procedure was used to create a map of GNPs based on their reflectance spectra within the sample.

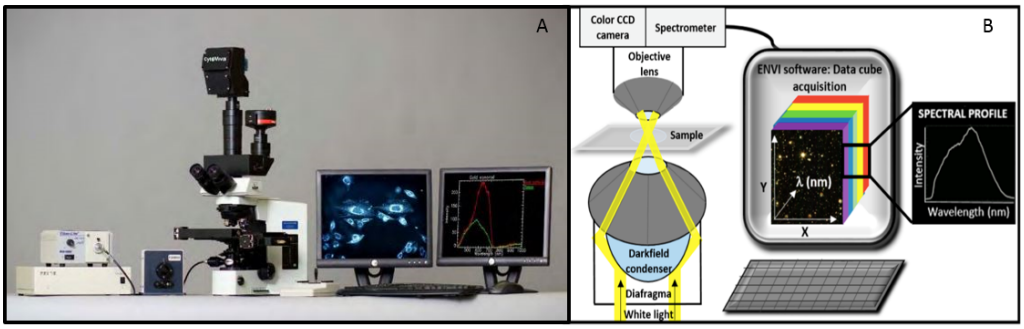

Figure 14. Cyto-Viva optical microscope. A) An image of the microscope, and B) Schematic diagram of the main optical components used for imaging (CC BY 4.0) [49].

In a spectral profile collected components of cells exhibit a flat scattering spectrum; GNPs show a sharp peak that depends on GNP size. CytoViva Hyperspectral Imaging System (CytoViva Inc., Auburn, AL, USA) was used to collect images and spectral profiles visualized with ENVI 4.8 software (Exelis Visual Information Solutions, Boulder, CO, USA). Acquisition time was dependent on required exposure time, to minimize noise and not have any overexposure and was typically a couple of minutes. Spectral resolution was 2.50 nm and range was 400 nm – 1000 nm. The pixel size for this system is 6.45 μm x 6.45 μm.

2.5 Cell culture and synchronization

MBA-MB-231 breast cancer cells were cultured in Dulbecco's Modified Eagle Media (DMEM)/HIGH GLUCOSE (HyClone) media, with 10% Fetal Bovine Serum (FBS) and 1% Penicillin-Streptomycin.. Penicillin and streptomycin are antibiotics used to prevent bacterial contamination of cell culture. Cell cycle analyses of three control samples are shown in **Figure 15**. Propidium Iodine staining indicates the DNA content in the cell. The large G0/G1 peak is when the cell has one copy of DNA, then in S phase DNA replication is occurring and the DNA content is somewhere between 1 and 2 copies. Finally in G2/M peak as the cell is preparing to divide there are two copies of DNA and therefore the propidium iodine staining is twice as high. The main goal of this thesis work was to synchronize the cells and investigate uptake and radiation dose enhancement.

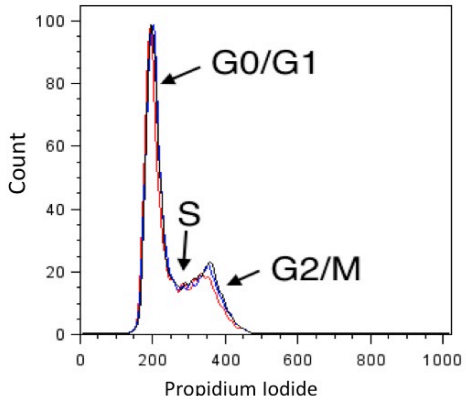

Figure 15. Propidium Iodine based cell cycle analysis. Quantification of DNA content in a control (unsynchronized) sample where cells are different stage of the cell cycle. The curves

marked in black, blue, and red represent analysis of three different control cell samples. Different phases of the cell cycle are identified as S, G0/G1, and G2/M.

Cell synchronization was done using double-thymidine block method [50]. Thymidine inhibits DNA synthesis and arrests cells in S phase. However, a double thymidine block ensures that any cells that were in mid or late S phase during the first block will be captured in late G1 or early S phase in the second block. MDA-MB-231 cells were seeded in a 6 well plate at 40% confluency, which means 40% density on the plate ($1.3x10^5$cells). Once the cells were settled and adherent to the dish, they were washed with Phosphate Buffered Saline (PBS) followed by adding 3ml 2 mM thymidine DMEM + 10% FBS + 1% PenStrep. After 26 hours, each well was washed twice with PBS and in regular DMEM for 16 hours. Following the wash, second thymidine block was carried out using 2mM Thymidine DMEM + 10% FBS + 1% PenStrep for 24 hours for fully synchronization of the cell population in S phase.

Synchronization of the population was verified using flow cytometry and propidium iodine staining [51, 52]. At desired time points, cells were harvested and a single cell suspension was prepared in buffer (PBS+ 2%FBS). Cells were washed with PBS and centrifuged at 300xg (300 times the acceleration of gravity) for 5 min twice. The cell pellet was then re-suspended in 1% PFA/PBS and incubated on ice for 15 minutes. This was the fixation step. Cells were again washed in PBS and centrifuged at 350xg for 5 minutes. Cells were re-suspended in 0.6 mL PBS and 1.4 mL freezer cold 100% ethanol (overall 70% ethanol). Samples were incubated in the dark at 4 degrees for at least an hour. This would further fix and dehydrate the cell sample. Samples were then centrifuged at 350xg for 10 minutes at 20 degrees. Cell pellet was re-suspended in 1ml PBS/ Bovine Serum Albumin (BSA) (0.5% BSA) and centrifuged at 350xg for 5 minutes at 20 degrees. To permeabilize the cell membrane and degrade RNA, cell pellet was re-suspended in PBTB (PBS, 0.5% BSA, 0.1 % Triton-X 100) followed by addition of RNaseA (100 ug/mL). Samples were left to shake at 37 degrees for 25 minutes. For labeling DNA, tubes were covered in foil, propidium iodide added (1:100 from 1 mg/mL), and incubated on shaker at 4 degrees for at least 1 hour. The cells were then centrifuged at 350 g for 5 minutes at 20 degrees. Finally PI stained cells were re-

suspended in 1 ml of PBS/BSA and passed the solution through a 50 μm cell strainer before running on Flow Cytometer. Measurements were done using BD FACSCalibur. Propidium iodide is highly fluorescent at 488 nm with broad emission centered around 600 nm. The amount of DNA content indicates which phase the cell population is in; this was how synchronization was verified.

2.6 GNP uptake

Once cells were in culture and had reached a confluency of approximately 70% in 6-well plates, different gold nanoparticle systems were added to fresh media at a final concentration of 0.2 nM and incubated for 20 hours in incubator at 37°C and 5% CO_2. Samples were prepared in triplicate.

2.7 Quantification of uptake in cells

2.7.1 Inductively coupled plasma mass spectrometry (ICP-MS)

The accumulation of GNPs in cells was analyzed using inductively coupled plasma mass spectrometry (ICP-MS). ICP source converts the atoms of the elements in the sample into ions, which are separated and detected using a mass spectrometer.

Following a 20-hour incubation with GNPs, cells were washed three times with PBS, so ensure any remaining gold in the media is removed. The cells were then harvested into a single cell suspension using Trypsin 0.25% (HyClone), and concentration of cells determined using Beckman Coulter Z2 Particle Counter and Size Analyzer. For ICP-MS analysis process, the cells needed to be digested and this was done using Aqua Regia in 3:1 ratio HCl:HNO_3, in an oil bath at 200°C. The samples were diluted and concentrations of gold (Au) atoms were measured in ppb with the Thermo X-Series II (X7) quadrupole ICP-MS instrument. A calibration curve was created using standards prior to sample measurements.

The following equations were used to calculate the number of GNPs of each sample from the concentration of Au atoms measured from ICP-MS:

$$\boldsymbol{Number\ of\ Au\ atoms\ per\ GNP\ (U)}$$

$$= \frac{Number\ of\ Atoms\ per\ unit\ cell\ (*) \times Volume\ of GNP\ (sphere)}{Volume\ of unit\ cell}$$

$$= \frac{4 \times \frac{4\pi\left({}^{D}/_{2}\right)^{3}}{3}}{a^{3}} = \frac{2}{3}\pi\left(\frac{D}{a}\right)^{3}$$

where D = core diameter of GNP, a = length of a unit cell = 4.08 Å = 0.408 nm

* Gold nanoparticles synthesized through salt reduction methods assemble into Face-Centered Cubic (FCC) structures and FCC lattices contain 4 atoms per unit cell (a unit cell refers to the smallest repeating structure of any solid used to simplify the crystalline patterns solids arrange themselves to a lattice) [53].

$$\boldsymbol{Number\ of\ GNPs\ for\ each\ sample}$$

$$= conc. measured\ from\ ICP\ MS\ \left[\frac{g}{L}\right] \times volume\ measured(L)$$

$$\times \frac{1}{molar\ weight\ of\ Au}\left[\frac{mol}{g}\right] \times Avogadro's\ number\ \left[\frac{Au\ atoms}{mol}\right]$$

$$\times \frac{1}{U}\left[\frac{GNP}{Au\ atoms}\right]$$

The number of GNPs per cell is then determined by dividing the number of GNPs by the total number of cells for that sample. This calculation assumes a homogenous distribution of GNPs in the cell population [39].

2.7.2 Graphite furnace atomic absorption (GFAA)

Following GNP incubation samples were processed the same as above in section 2.7.1. GFAA is another spectrophotometry technique. Atomic absorption is based on the reduction of intensity of electromagnetic radiation from a light source after passage through a cell containing gaseous atoms [54, 55]. A small amount of sample is placed inside a hollow graphite tube. The graphite furnace heats the analyte in a temperature program and converts the liquid or solid samples into gaseous atoms[54]. A continuum light source emits a wide range of wavelengths, enters the cell containing the analyte. In

absorption the transfer of energy from a photon to an atom requires the energy of the photon to be identical to the difference in energy between the energy electron levels of the atom. An individual monochromatic light beam with intensity I_o enters, and transmitted light passes through a monochromater and detector measuring the intensity I. Each element has a unique set of electron orbital energy level, giving a unique spectra allowing for specific quantification of a particular element, in this case gold [54] Transmission is described as the ratio of intensity of light after and before passing through the sample:

$$T = \frac{I}{I_o}$$

The amount by which light is diminished is proportional to the number of atoms. Absorption is written as:

$$A = -\log T = \log \frac{I_o}{I}$$

Absorbance vs. concentration gives a straight line. Therefore standards of known concentration are analyzed so that the concentration of samples based on the absorption measured can be calculated.

Agilent Technologies Graphite Tube Atomizer (GTA) 120 was used for these assays. Sample cups were rinsed with 10% HCl and dried prior to loading sample. Following the programmed data collection, a concentration in μg/ml was determined and calculations to determine the number of GNPs were conducted as in previous section.

2.8 Irradiation plan and delivery

Treatment planning was done using Eclipse [Varian Medical Systems, Palo Alto] treatment planning system at BC Cancer Victoria as shown in **Figure 16**. Tissue culture dishes were placed between two 5 cm thick solid water (water equivalent plastic) blocks that were 40 x 40 cm^2. A single field was planned, with a gantry rotation of 180° so the small air gap between the top of the media and top of dish is less significant. A field size of 28 cm x 28 cm was used. SAD of 100cm was set up such that the axis was right at the

bottom of the dish where the cells were located. Dose rate was 600 MU/min. With the reference point at isocenter at a depth of 5.0cm the dose coefficient is 100.95 MU/Gy.

$$\text{MU setting} = \text{prescribed dose(Gy)} \times \text{dose coefficient}\left(^{\text{MU}}/_{\text{Gy}}\right)$$

$$= \frac{\text{prescribed dose}}{\text{RDR}\times S_c \times S_p \times \text{TMR}}$$

RDR = reference dose rate = 1cGy/MU

TMR = tissue maximum ratio = TMR (6MV, 28x28, d=5) = 0.925

S_c = collimator scattering factor = 1.038

S_p = phantom scatter factor = 1.032

Typical dose in clinical treatment is done in 2 Gy fractions; therefore in this study a dose of 2 Gy was used. The radiation type selected was 6 MV photons; this again was to be similar to energies used in clinics. Therefore to achieve a dose of 2 Gy at the reference point 202 MU were delivered, in a treatment time of about 40 seconds.

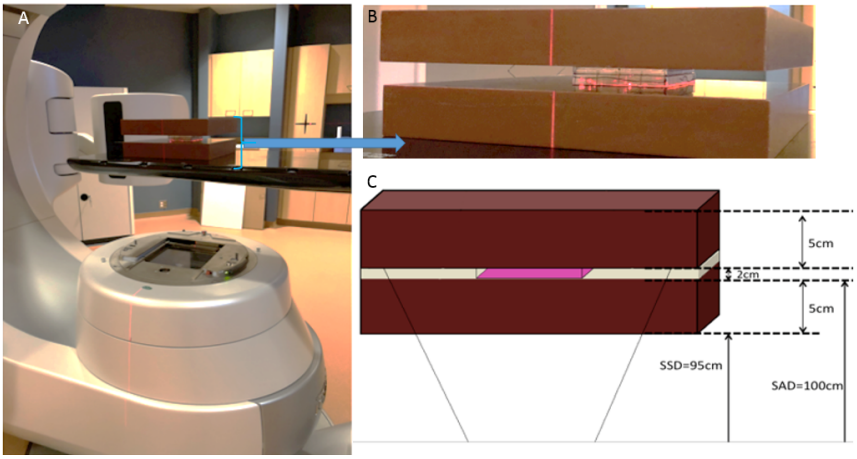

Figure 16. Cell irradiation set up. A) Linear accelerator, B) Closer look at the sample in between solid water, and C) Dimensions of the set up as outlined in table 1.

Table 1 Linear accelerator set-up parameters

Set-Up Parameter	Value
Gantry Rotation	180.0°
Collimator Rotation	0.0°
X Field Dimension	28.0 cm at isocentre
Y Field Dimension	28.0 cm at isocentre
SSD	95.0 cm
SAD	100.0 cm

2.9 Clonogenic assay

Protocol for clonogenic assay was performed as described in "Chemosensitivity In vitro assays". [56]After the treatments, the cells were trypsinized and diluted to form single-cell suspensions. Cell concentrations were determined by counting using hemocytometer. The required volumes of cell suspension solution were calculated for the control and treatment samples. The calculated volume of cell suspension for each condition was seeded in 60 mm tissue culture dishes in triplicate. 200 cells were plated for un-irradiated conditions and 400 cells for those that received 2 Gy. The cells were left in the 37 °C humidified incubator with 5 % CO_2 for 14 days for colonies to grow. Once colonies were formed, the dishes were stained and fixed with 0.1 % of methylene blue (BioShop) in 70 % ethyl alcohol for 1 hr. The stained dishes were rinsed in lukewarm water and left to air-dry overnight. The air-dried control dishes were then counted. Colonies were defined as structures containing >50 cells. Then the plating efficiency (PE) was obtained.

$$PE = \frac{Number\ of\ colonies\ counted}{Number\ of\ cells\ plated}$$

The colonies of treatment samples were also counted and the survival fraction (SF) was obtained with the following equation:

$$SF = \frac{Number\ of\ colonies\ counted}{Number\ of\ cells\ plated \times PE}$$

2.10 DNA damage staining

MDA-MB-231 cells were grown directly on glass coverslips in 6-well dishes. 24 hours following treatment with GNPs and irradiation, cells were fixed with 2% paraformaldehyde/0.2% Triton-X 100 for 20 minutes at room temperature (PFA) (Sigma-Aldrich). Each well was then washed 3 times in PBS for 5 min. Cells were then treated with 0.1% Triton-X for 20 minutes at room temperature. Then again were washed 3 times in PBS for 5 minutes. Cells were incubated with 3% BSA (Bovine Serum Albumin) for

one hour. Coverslips were then placed face down on Para film with a 50ul drop of primary antibody 1:800 (gammaH2AX Ser 139. Millipore 05-363 Lot 2276332) in 3% BSA/PBS and incubated overnight at 4°C. Coverslips were washed with 0.5% BSA/ 0.175% Tween 20/ PBS 3 times for 5 minutes. Secondary antibody was diluted 1:500 (anti-mouse IgG Alexa 647. Life Technologies Ref A31571, Lot423849) in 3% BSA/PBS and coverslips incubated for 45 minutes. Coverslips were again washed with 0.5% BSA/ 0.175% Tween 20/ PBS 3 times for 5 minutes, then PBS 3 times for 5 minutes. Coverslips were mounted on glass coverslips with a drop of Vectashield containing DAPI. The top of the coverslip was gently pressed down and the edges of the coverslip sealed with nail polish.

2.10.1 Confocal imaging

Fluorescently labeled MDA-MB-231 cells were mounted on glass microscope slides as described in section 2.11 and imaged using Nikon Confocal microscope and NIS-Elements Software. For DAPI stain a 405 nm laser was used and for gammaH2AX a 640 nm laser at 15% power. Images were acquired using 60X objective and taken as a Z-stack that was then projected into a single plane. Z-stack settings were such that each step was 1.5 μm and 10 steps were recorded to ensure the entire cell is imaged top to bottom.

2.12 Statistical analysis

Data was collected in triplicate for each experiment and results are displayed as mean ± standard error. Statistical analysis was performed using IBM SPSS Statistics software. To determine the statistical significance between pairs of results two-sample t-test was used. A p-value of less than 0.05 was considered to be significant.

Chapter 3
Results & Discussion I: Functionalized gold nanoparticles

Inorganic NP systems are fairly easy to synthesize and design, especially in the case of GNPs whose size and surface are easily modified. The citrate reduction method of synthesis only requires varying concentrations of sodium citrate, which acts as a reducing and coating agent. The citrate molecules can be easily removed by other functional molecules that contain a thiol (S) at the end since gold-thiol bond is favoured and strong. Hence, molecules that have a thiol ending were chosen for functionalization of GNPs. One of the molecules selected for functionalization was thiol terminated polyethylene glycol (PEG) of molecular weight 2k Da. Polyethylene glycol has promoted the prospective applications of nanoparticles (NPs) in cancer therapy. PEG is used to evade the immune system allowing NP accumulation within the tumour using its leaky vasculature. However, the cellular uptake of PEG-coated (PEGylated) NPs is lower in comparison to non-PEGylated NPs since PEG minimizes surface binding of ligands that mediate NP endocytosis [57]. For improved outcome in therapeutic applications, it is necessary to enhance the uptake of PEGylated NPs. A peptide (CKKKKKKGG**RGD**MFG) containing an integrin-binding domain was added to the NP surface in addition to PEG. The cysteine at the end of this peptide sequence facilitates the binding onto GNP surface. The molecular weight of the peptide is 1669 Da.

3.1 Characterization

GNPs of sizes 15 nm and 46 nm were used in this study. Ultraviolet Visible (UV-Vis) spectroscopy, DLS, zeta potential, dark-field and hyperspectral imaging were the methods used for characterization of these NP complexes.

3.1.1 Ultraviolet-Visible spectroscopy

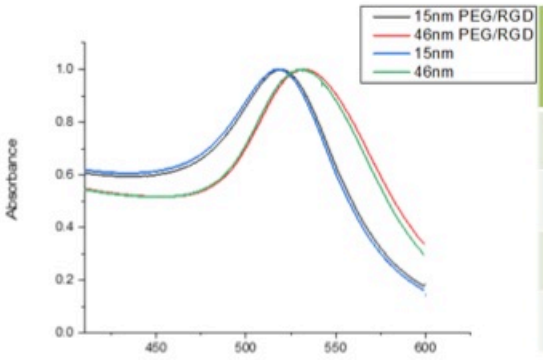

Surface Ligand	Peak Wavelength (nm)	
Size of GNPs (nm)	15	46
As-made	517	532
GNP PEG	519	533
GNP PEG/RGD	529	533

Figure 17 . UV-Vis spectrum for 15 nm and 46 nm GNPs**.**

Figure 17. shows the UV-Vis data for as-made GNPs and functionalized GNPs. 15 nm as-made (unmodified) GNPs had an absorption peak wavelength at 517 nm. The addition of PEG/RGD molecules shifts the peaks to 519 nm. The shift in the peak wavelength indicates that the functionalization molecules are attached to the NP surface. Similar response was seen with GNPs of diameter 46 nm. GNPs (unmodified) of diameter 46 nm had a peak wavelength at 532 nm. Addition of PEG and RGD peptide on to GNP surface shifted the peak wavelength slightly to 533 nm. This is consistent with what was observed with 15 nm GNPs. Binding of ligands to GNPs is known to red-shift by a few nm. This shift is a result of an increase in local refractive index at the gold nanoparticle surface.

3.1.2 Dynamic light scattering and zeta potential

Both dynamic light scattering (DLS) and zeta potential measurements were done to further verify the functionalization of GNP surface and also to confirm that NP complexes were not aggregated. Dynamic light scattering uses light scattered by particles in solution to gain information about their motion. The fluctuations in intensity as the

particles undergo Brownian motion were used to compute the intensity correlation function and determine a diffusion coefficient. The hydrodynamic diameter was then calculated, which depends on the size and shape of the particles.

A

Surface Ligand	Hydrodynamic Diameter (nm)	
Size of GNPs (nm)	**15**	**46**
As-made	19.7 ± 1.7	52.5 ± 1.3
GNP PEG/RGD	22.8 ± 1.5	54.1 ± 1.6

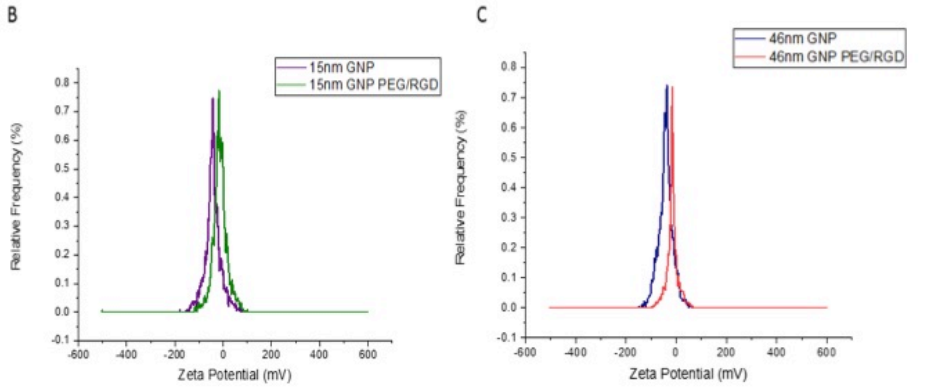

Figure 18. Dynamic light scattering and zeta potential measurements of GNPs. A) Dynamic light scattering measurements for 15 and 46 nm GNPs, B-C) Zeta potential measurements for 15 and 46 nm GNPs with and without surface modification of PEG/RGD, respectively.

Hydrodynamic diameter can be defined as the diameter of a hypothetical sphere that diffuses at the same rate as the particle under investigation [58]. The average hydrodynamic diameter for 15 nm GNPs was 19.7 nm. Following functionalization of the GNPs and addition of PEG/RGD the hydrodynamic diameter increased slightly due to the increase in size. The molecules added were smaller and the increase in size was that significant as shown in **Figure 18**. Similarly, the average hydrodynamic diameter for 46 nm GNPs was 52.5 nm. Following functionalization of the GNPs and addition of

PEG/RGD the hydrodynamic diameter increased slightly due to the increase in size for the same reasons discussed for 15 nm GNPs.

Zeta potential measurements (see **Figure 18 (B-C)**) also gave a measure of the stability of the particles in solution. More negative surface charge means that the particles will repel one another and not form aggregates. Mean zeta potential for 15 nm GNPs was negative and it was -43.7±1.9 mV. The zeta potential measurement shifted to -16.1±1.3mV once PEG/RGD was added. The reduction in the surface charge was expected since RGD peptide has a positive charge and PEG is neutral. Zeta potential value for 46 nm GNPs was measured to be -32.9±1.4 mV. The addition of PEG/RGD resulted in a less negative value of -14.8±0.7mV. This is consistent with the results obtained for 15 nm GNPs. However, the presence of overall negative charge in these functionalized NPs led to their stability in solution.

3.1.2 Dark-field and hyperspectral imaging

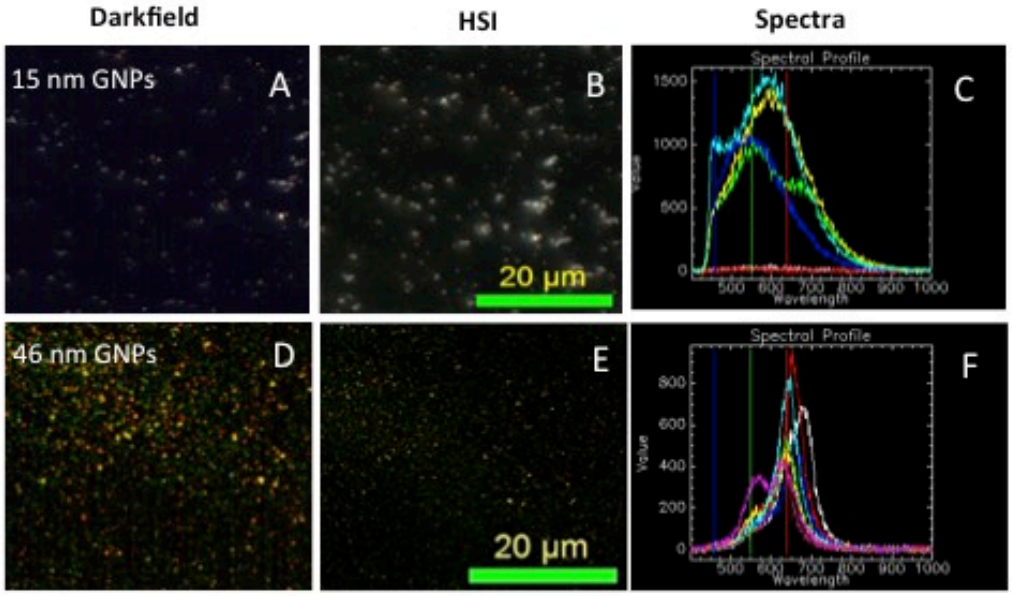

Figure 19. Dark-field and hyperspectral imaging of functionalized GNPs. A-C) 15 nm PEG/RGD GNPs; A) Dark-field image, B) Hyperspectral image, and C) a collection of spectral profiles of different pixels in the hyperspectral image. D-F) 46 nm PEG/RGD GNPs; D) Dark-field image, E) Hyperspectral image, and F) a collection of spectral profiles from different pixels in the hyperspectral image.

This Cyto-Viva technology was specifically designed for optical observation and spectral confirmation of NPs as they interact with cells and tissues. With the integrated CytoViva hyperspectral imaging capability, reflectance spectra from specific materials can be captured and measured. Dark-field and hyperspectral images of 15 nm GNPs and 46 nm GNPs along with few corresponding spectra are shown in **Figure 19**. In hyperspectral imaging, each pixel of the image collected also contains spectral information. Therefore without any fluorescence labelling GNPs can be identified and characterized.

3.2 Uptake of functionalized gold nanoparticles

In the following section only GNPs functionalized with PEG/RGD are discussed. The comparison to "as-is" GNPs and optimization of functionalization have been done in previous studies, and in chapter 5 of this thesis, results for GNPs in MDA-MB-231 cells is investigated in a synchronized cell population [35, 57].

3.2.1 Quantification of functionalized nanoparticle uptake using inductively coupled plasma mass spectrometry

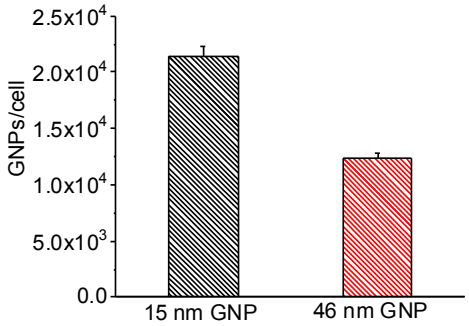

Figure 20. GNP uptake in MDA-MB-231 cells after 20-hour incubation of 0.2 nM PEG/RGD modified GNPs.

Inductively Coupled Plasma Mass Spectrometry (ICP-MS) analysis was done following a 20 hour incubation with GNPs of two different sizes: 15 nm GNPs with surface modification of PEG/RGD as well as 46 nm PEG/RGD GNPs. As shown in **Figure 20**, the number of GNPs accumulated per cell was 21,000 ± 900 for 15 nm GNPs and 12,000 ± 450 for 46 nm GNPs. Uptake was higher in 15 nm PEG/RGD GNPs compared to 46 nm. Even though grafting density of PEG was the same for both 15 and 46 nm GNPs, the protective force of the PEG molecules against surface bound peptides interacting with cell membrane receptors was greater for 46 nm GNPs than 15 nm ones. This could be due to the fact that larger NPs have lower surface curvatures than smaller NPs. Lower surface curvatures could lead to less free space between grafted molecules despite consistency in grafting distances. Less free space between PEG molecules reduces GNP surface interaction of RGD peptide with cell surface receptors. This explains the core size dependence of NP uptake when functionalized with PEG and RGD peptide.

3.2.2 Quantification of functionalized gold nanoparticles in cells with graphite furnace atomic absorption method

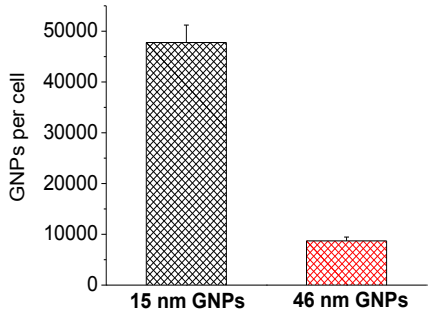

Figure 21. Comparison of functionalized PEG/RGD GNP uptake of small (15 nm) and large (46 nm) GNPs using Graphite Furnace Atomic Absorption analysis technique.

The cellular uptake of GNPs was quantified using Graphite Furnace Atomic Absorption (GFAA) technique in addition to ICP-MS and the results are shown in **Figure 21**. The results obtained using GFAA technique gave the same trend as the results obtained from ICP-MS. However, the number of NPs per cell and rate of decrease between 15 nm and 46 nm GNPs were different but the same trend was seen as with ICP-MS, with higher uptake occurring with 15 nm PEG/RGD GNPs.

3.2.3 Toxicity of functionalized PEG/RGD gold nanoparticles

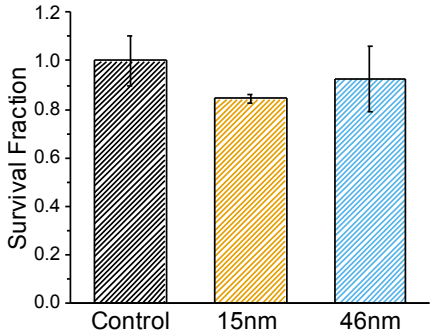

Figure 22. Survival fraction of MDA-MB-231 breast cancer cells following introduction of 15 nm and 46 nm PEG/RGD GNPs.

Gold nanoparticle system must be safe when introduced to cells in order to be considered as a potential radiosensitizer. There have been many reports that GNPs can be made such that they are non-toxic and biocompatible and any toxicity introduced due to GNPs depends on parameters such as the size, surface properties, and concentration [24, 34, 59]. To assure that our two systems did not introduce a significant amount of toxicity, clonogenic assays were performed and the results are shown in **Figure 22**. GNPs of size 15 nm functionalized with PEG/RGD showed a survival fraction (SF) of 0.85±0.02 while GNPs of diameter 46 nm with PEG/RGD had a SF of 0.93±0.13. Both conditions of small and large GNPs had no significant difference in SF compared to control cells with no GNPs ($p>0.05$).

3.2.4 Dark-field and hyperspectral imaging of cells internalized with gold nanoparticles

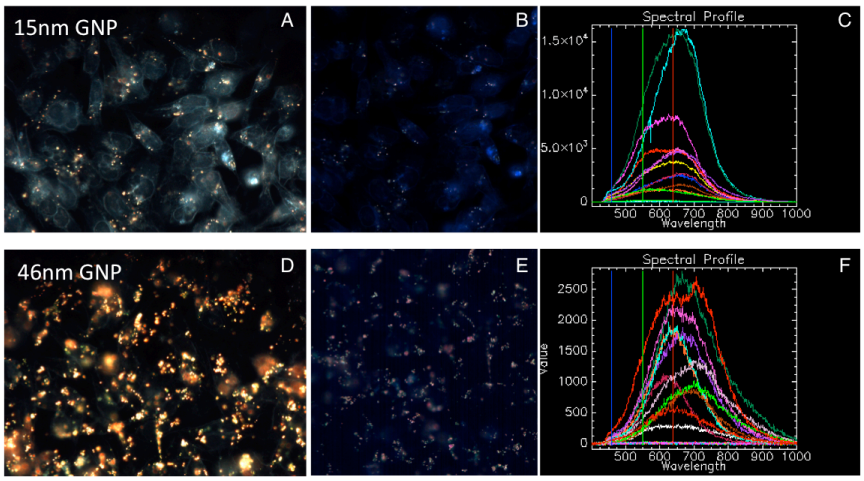

Figure 23. Dark-field and hyperspectral images of GNP in MDA-MB-231 cells. A-C) 15 nm GNPs in cells and D-F) 46 nm GNPs internalized in cells: A) Dark-field image, B) Hyperspectral image, and C) a collection of spectral profiles of different pixels in the image B; D-F) 46 nm GNPs in cells: D) dark-field image, E) hyperspectral image, and F) collection of spectral profiles of different pixels in the hyperspectral image.

Dark-field and hyperspectral imaging confirms the presence of GNPs in cells as shown in **Figure 23**. Gold nanoparticles enter the cell mostly *via* endocytosis and localize in small vesicles like endosomes and lysosomes as discussed before in the chapter 1. The bright dots seen in the cellular images may not represent single NPs and they could be clusters of GNPs localized in either endosomes or lysosomes. These clusters of GNPs appeared as very bright dots, especially the larger 46 nm GNPs. Although there are fewer 46 nm sized GNPs/cell, these nanoparticles contain 30 times more gold atoms than 15 nm GNPs.

3.3 Radiation Sensitization effect of gold nanoparticles

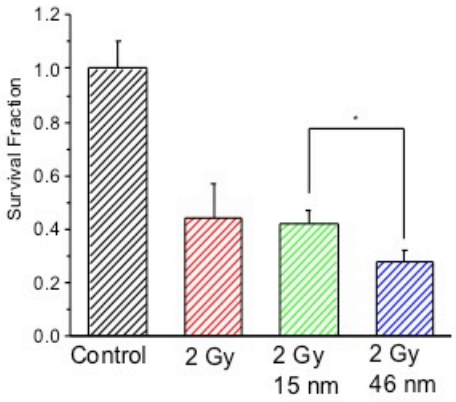

	Survival Fraction
Control	1 ± 0.10
2 Gy	0.44 ± 0.12
2 Gy 15 nm	0.42 ± 0.05
2 Gy 46 nm	0.28 ± 0.04

Figure 24. Survival fraction when MDA-MB-231 cells are incubated with GNPs and irradiated with 2Gy dose.

MDA-MB-231 cells were incubated for 20 hours with 15 nm and 46 nm GNPs functionalized with PEG and RGD. After the NP incubation, radiation dose of 2 Gy was given using a linear accelerator step up explained in chapter 2. The energy of the photons was 6 MV. As is typically done a clonogenic assay was performed to determine the outcome of the radiation treatment. The results are shown in **Figure 24**. The cells incubated with 15 nm GNPs prior to radiation had a 5% decrease in survival fraction as compared to control cells after receiving a dose of 2 Gy. In contrast, the cells treated with 46 nm GNPs showed 37% decrease in survival as compared to the control cells with no GNPs. Through statistical analysis, it was concluded that the difference in survival fractions between 15 nm GNPs and 46 nm GNPs is statistically significant ($p<0.05$).

3.4 Discussion

3.4.1 Rationale for using 15 nm and 46 nm GNP

Using the UV-Vis spectrum and dynamic light scattering distribution, the diameter of GNPs used in this study were determined to be 15 nm and 46 nm. Ultraviolet-Visible spectroscopy measures the Local Surface Plasmon Resonance (LSPR) and results in a strong absorbance band in the visible region 500 nm to 600 nm. As the gold nanoparticle diameter increases the peak wavelength increases. A small "red-shift" is related to the increase in size of nanoparticle, and is observed following the addition of PEG and RGD to the NP surface as explained by Mie theory [35]. Previous studies have shown that internalization of GNPs is dependent on size, with highest uptake occurring for GNPs with diameter 20-50 nm [34, 60]. Different cell lines were used in each study, so optimization of nanoparticle size also depends on cell line. Experiments done *in vitro* give an indication of how nanoparticles will interact with tumours on a cellular level, but in reality cancer cells in tumour tissue are surrounded by an extracellular matrix (ECM). For GNPs to reach tumour cells they will have to be capable of travelling through an imperfect blood vascular system, cross vessel walls and penetrate through multiple layers of tissue. Multicellular layer (MCL) models are created to include the extracellular matrix and simulate a reasonable tumour microenvironment [61]. Although 50 nm GNPs are preferentially taken up by MDA-MB-231 cells in a monolayer, when investigated in a multilayer system smaller GNPs were able to penetrate further through the tissue and at greater depth uptake of 20 nm GNPs was higher [62]. With the future goal of being able in introduce methods in this project to multi-layer systems, while also investigating effects on uptake at a monolayer level, the sizes chosen for this project were 15 nm and 46 nm diameter spherical GNPs.

3.4.2 GNP accumulation

Functionalizing GNPs with polyethylene glycol is very useful *in vivo*. PEG molecules allow the gold nanoparticle they surround to avoid detection by macrophages

in the immune system, increasing blood circulation time giving more opportunity for the particles to travel to the targeted tumour site [35]. However, the surface modification with PEG leads to a lower cellular uptake *in vitro* and *in vivo*. Several studies with different cell lines suggest that PEG-coated GNPs localize external to cancer cells. To improve nanoparticle uptake of PEGylated GNPs, peptides containing the integrin binding domain arginine-glycine-aspartic acid (RGD) were added to the surface. Studies by Chithrani *et al.* showed highest cellular uptake of 50 nm GNPs that were not functionalized [34]. With PEG/RGD surface modifications and a 20-hour incubation of 0.2 nM GNPs with MDA-MB-231 cells the number of GNPs accumulated per cell was 21,000±900 for 15 nm GNPs and 12,000±450 for 46 nm GNPs. These results are in agreement with what Cruje *et al.* described; they saw an improvement in uptake in smaller GNPs functionalized with PEG/RGD compared to PEG alone. The difference here compared to the previous study completed by Cruje *et al.* is the concentration of GNPs used in this thesis is 10-times higher; 0.2 nM compared to 0.02nM. Survival data in Figure 24 shows that cells treated with 46 nm GNPs have a lower survival as compared to 15 nm GNPs. However, the study done by Cruje *et al*. had the opposite result where cells treated with 15 nm GNPs had a lower survival as compared the cells treated with 50 nm GNPs. We believe that the change in concentration by 10-fold in our case resulted in more 46 nm within cells that led to lower survival. For example, ratio of 15:46 GNPs in our study is ~ 1:2 while it was 1:5 in the study done by Cruje *et al*. Experimental data in this thesis illustrated in Figure 24 is supported by the theoretical survival fractions calculated using MC simulations that were performed, but are not shown. The lower uptake of PEG and RGD peptide modified 46 nm GNPs as compared to the smaller 15 nm ones is due to the accessibility of RGD to surface proteins on the cell [35]. The smaller radius of curvature of 15 nm GNPs compared to 46 nm, opens up space for the RGD peptide to reach the surface receptors.

The investigation into using graphite furnace atomic absorption was done to confirm if another analysis method would result in the same trend of PEG/RGD GNP uptake, with higher uptake seen with smaller 15nm functionalized GNPs. Although there was a difference in the scale, results show what was seen previously with ICP-MS analysis as well as results from other groups [35].

To determine if our gold nanoparticle systems showed any toxicity, clonogenic assays were performed after 20 hours incubation with a concentration of 0.2 nM. As illustrated in **Figure 22**, these nanoparticles did not cause any statistically significant cytotoxicity at the concentrations used. The concentration of 0.2 nM used in this study is the lower end of concentrations used in GNP radiosensitization experiments [23].

Dark-field and hyperspectral imaging gave confirmation that GNPs were internalized within the cells and their distribution within cells. Although there were more GNPs per cell for 15 nm GNPs, because 46 nm GNPs are larger, there is more gold in the cell. This was seen as all of the bright spots in **Figure 23**. This could explain the radiation sensitization results. There was more gold inside cells incubated with 46 nm GNPs leading to higher enhancement of cell killing. The decrease in survival was 37% for cells treated with 46 nm GNPs *vs.* 5% for cells treated with 15 nm GNPs.

Chapter 4
Results & Discussion II: Lipid nanoparticles encapsulating small gold nanoparticles

Researchers around the world have dedicated their careers to developing more efficient cancer treatments and to reduce adverse effects caused by current available therapies. Nanotechnology based platforms, such as micelles, polymers, liposomes, solid lipid nanoparticles, and metal nanoparticle-conjugated biodegradable systems, have been proposed for use in improved cancer chemotherapy [63]. Lipid nanoparticles are the simplest artificial biological cells; they are made up of natural lipids, usually phospholipids and cholesterol, which can encapsulate molecules in hydrophilic or hydrophobic core.

Heavy elements such as gold with atomic number of 79 have been investigated as radiosensitization agents in radiation therapy treatments due to its ability to absorb more radiation per unit mass than soft tissue, high density targeting capability and biocompatibility [15]. Small gold nanoparticles (1-10 nm) are not well internalized by cells on their own, the mechanism of internalization has been seem to favour larger particles with highest uptake occurring for particles with a diameter of 50 nm [34]. Therefore how a system of 50 nm lipid nanoparticle (LNP) encapsulating small 5 nm gold nanoparticles (GNPs) would affect uptake was investigated. Using lipids for surface coatings or encapsulations of metallic nanoparticles is a good way to increase biocompatibility, as the surface chemistry of the lipids is similar to structural components of the cellular membrane [64]. **Figure 12** is a schematic diagram explaining the concept of encapsulation of small GNPs in a LNP system.

Lipid nanoparticles are also of interest as a carrier for gene and drug delivery [65]. Approximately one third of potent anti-cancer drugs are hydrophobic causing toxicity due to their low solubility. Drug encapsulation in lipid nanoparticles could be a method to overcome systemic toxicity of these drugs and create opportunity to combine with radiosensitizing GNPs and label to target tumour cells specifically [66].

4.1 Characterization of lipid nanoparticles

Two lipid nanoparticle formulations were tested for this study. They are LNP-A and LNP-B. The difference between these samples was the number of small GNPs encapsulated. Ultraviolet Visible (UV-Vis) spectroscopy, transmission electron microscopy (TEM), dark-field & hyperspectral imaging were used for characterization of these NP formulations.

4.1.1 Lipid nanoparticle size and shape

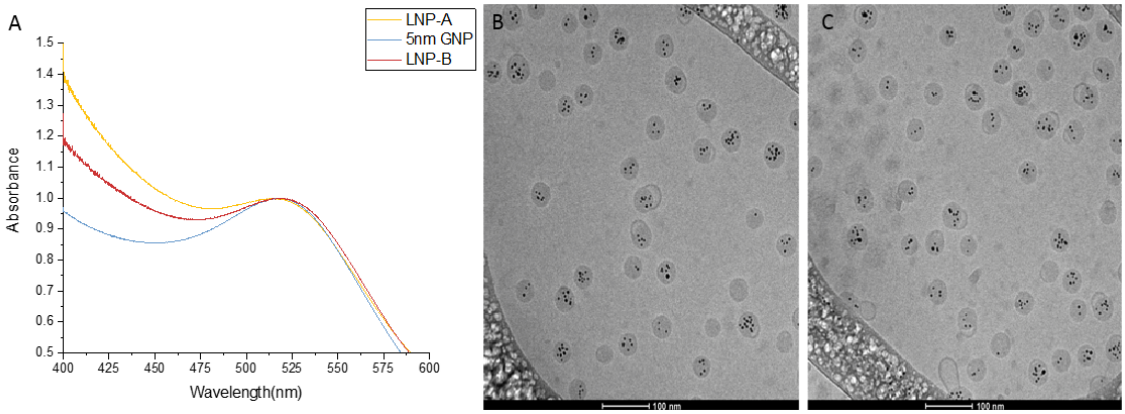

Figure 25. Characterization of lipid nanoparticles. A) UV-Vis spectrum for 5 nm GNPs and lipid nanoparticle formulations LNP-A and LNP-B. Normalized to the peak wavelength of 519 nm. B-C) TEM images of LNP-A and LNP-B. The scale bar is 100 nm.

Figure 25 shows the UV-Vis spectra of lipid nanoparticles (LNP) containing 5 nm gold nanoparticles and GNPs alone in solution. UV-Vis spectroscopy measures the Local Surface Plasmon Resonance (LSPR). The peak wavelength for 5 nm GNP spectrum is at 519 nm. The spectroscopic properties of the nanoparticle solution can provide an indicator of their size distribution by fitting the position of the surface plasmon resonance to a simple wavelength function [67]. Lipid nanoparticle formulations A and B had 5 nm GNPs encapsulated in the core as shown in TEM images of **Figure 25**. Both LNP-A and LNP-B formulations also had a peak at 519 nm indicating the presence of small GNPs within lipid NPs. However, these UV spectra are normalized and it was

noticed that the concentration, of GNPs within LNPs was lower compared to same concentration of smaller GNPs.

The shape and size of lipid nanoparticles with small gold nanoparticles (5 nm diameter) encapsulated was also determined with TEM (see **Figure 26**). These images were used to confirm the size of LNP was 50 nm in diameter and to visualize the distribution of 5 nm GNPs within the LNPs. It was determined that there was an average of 1.5 ± 1.5 gold nanoparticles per LNP in formulation A and 5.0 ± 4.8 gold nanoparticle per LNP in formulation B.

4.1.2 Calculating the concentration of lipid nanoparticles

To form lipid nanoparticles (LNPs), lipids are initially dissolved in ethanol and the small 5nm GNPs were suspended in 25 mM sodium acetate. The organic and aqueous phase were mixed through a T-junction mixer. The concentration of lipid nanoparticles in the resulting solution was very difficult to measure, however, an attempt was made to come up with an estimate. The concentration of LNP/ml could be calculated because a few values were available from the LNP synthesis process:

Diameter of LNP = 50 nm

Lipid density = 0.9 g/ml

Molecular Weight = 590 g/mol

Bilayer Thickness = 3 nm

Surface Area per lipid = 0.7 nm^2

A calculation was done first to determine how many lipids were used to form the LNP. It was used to calculate how many LNPs were formed.

Calculated volume of the interior of the LNP:

$$V = \frac{4}{3}\pi(22\ nm)^3 = 44602\ nm^3$$

$$44602 nm^3 * \frac{10^{-21}\ ml}{nm^3} * 0.91 \frac{g}{ml} * \frac{mol}{590\ g} * 6.022 * 10^{23} \frac{molecules}{mol}$$

$$= 41413\ molecules$$

The surface area (SA) of the LNP formed is:

SA of LNP= $4\pi(25nm)^2 = 7853nm^2$

$$7853\ m^2 * \frac{lipid}{0.7\ nm^2} = 11220\ lipids$$

$$Lipids\ per\ LNP = 41413 + 11220 = 52633\ \frac{lipids}{LNP}$$

Formulation A had 9.1 mg/ml of lipid and the concentration if LNP-A was as follows:

$$9.1\frac{mg}{ml} * \frac{mol}{590g} * 6.022 * 10^{23}\frac{lipids}{mol} * \frac{LNP}{52633\ lipids} = 1.76 * 10^{14}\frac{LNP}{ml}$$

4.1.3 Dark-field and hyperspectral imaging of lipid nanoparticles

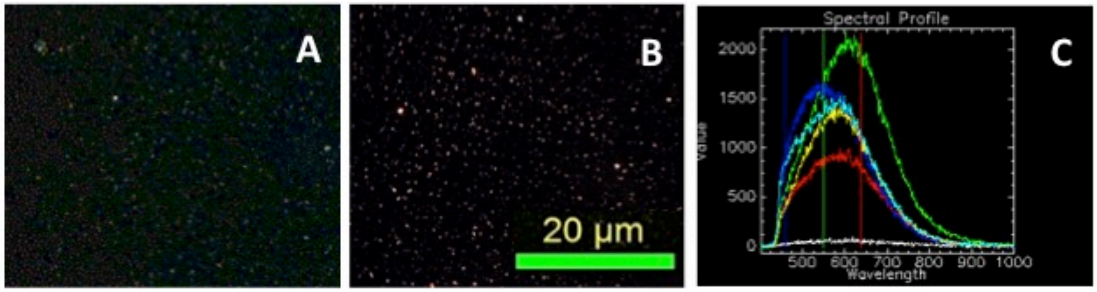

Figure 26. Spectra of gold nanoparticles encapsulated in LNP. A) Dark-field image of LNP-A, B) Corresponding Hyperspectral Image, and C) Spectra of pixels showing profile of GNPs in LNP

Figure 26. illustrates the dark-field and hyperspectral images of 50 nm LNPs with 5 nm gold nanoparticles encapsulated within. Each of the bright dots in the image is a LNP. Metal nanoparticles scatter and absorb light in a precise way enabling quantitative spectral analysis. Each pixel of a hyperspectral image contains a spectral profile, allowing for identification of the characteristic spectrum of GNPs, which depends on size of GNP. By collecting spectra of different LNPs, it was confirmed that not all of the LNPs contain gold. The flat spectrum in **Figure 26C** shows a spectrum from a LNP with no GNPs. The small gold nanoparticles have a spectral peak around 650 nm.

4.2 Toxicity of lipid nanoparticles

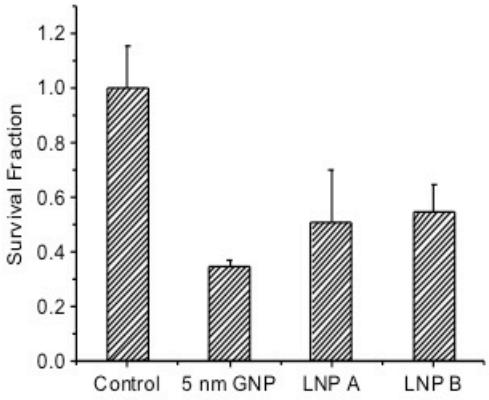

	Survival Fraction
Control	1 ± 0.15
5 nm GNP	0.35 ± 0.02
LNP A	0.51 ± 0.18
LNP B	0.54 ± 0.10

Figure 27. Toxicity due to nanoparticles. Survival fraction for MDA-MB-231 cells incubated with 5 nm GNPs, and lipid nanoparticle formulation A and B.

A clonogenic assay was used to determine the toxicity introduced by these NPs to cells. The concentration of NPs used was 0.2 nM and results from our clonogenic assay are shown in **Figure 27**. It clearly shows that 5 nm GNPs introduced the highest toxicity after incubation period of 20 hours in MDA-MB-231 cells. Encapsulation of these 5 nm GNPs in LNPs reduced the toxicity about 20%. However, the survival fraction of cells treated with LNP-A and LNP-B were still about 50%, which may not be yet acceptable as a GNP delivery system. This was one of the reasons that it was decided not to continue investigating LNPs until GNP encapsulation has been optimized and the related toxicity issues resolved. One possibility for toxicity may be due to the fact that LNPs which are internalized in MDA-MB-231 cells begin to degrade within the cells releasing small 5 nm GNPs into cytoplasm. This could cause the toxicity similar to what was seen with 5 nm GNPs alone [68, 69]. However, because toxicity was reduced with LNP compared to small 5 nm GNPs alone, uptake and the radiation dose enhancement in cells treated with LNP-A and LNP-B were also investigated as discussed in the next section.

4.3 Uptake of lipid nanoparticles in breast cancer cells (MDA-MB-231)

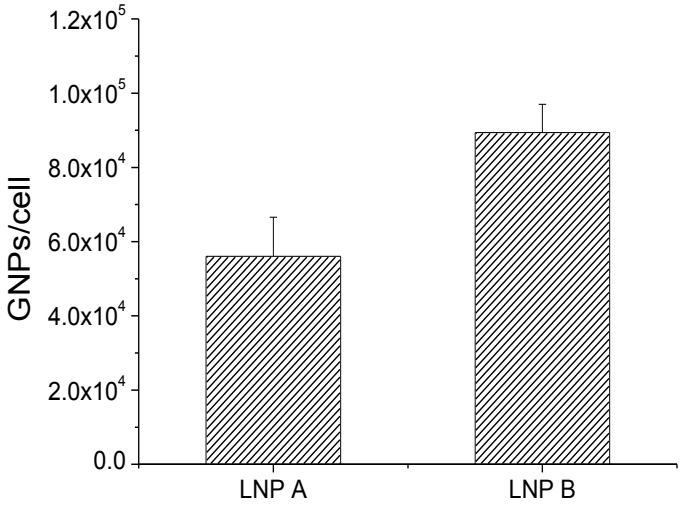

Figure 28. Cellular uptake of lipid nanoparticle formulations, LNP-A and LNP-B.

MDA-MB-231 cells were incubated with a 0.2 nM concentration of two formulations of LNP-A and LNP-B separately for 20 hours. **Figure 28** shows uptake of GNPs encapsulated in 50 nm LNPs is 56031 ± 10554 GNP/cell for LNP-A and 89362 ± 7623 GNP/cell for LNP-B. Lipid nanoparticle formulation A has an average of 1.5±1.5 GNP per LNP. A higher uptake of LNPs was expected than what was observed because 50 nm NPs have a greater internalization in cells than smaller NPs as discussed in the section 1.5. It could be explained by there being a higher uptake of LNPs, however, some of the LNPs could be empty. Hence it is not very surprising that its uptake is the lower. The entrapment efficiency was better for LNP-B formulation since it had 5.0±4.8 GNP per LNP. As expected, there was an increase in the GNPs within cells treated with LNP-B.

Figure 29 shows the dark-field and hyperspectral imaging of LNPs alone. The same dark-field and hyperspectral imaging was used to probe LNPs localized in MDA-MB-231 cells. **Figure 29 (A-B)** illustrates the dark-field and hyperspectral images of

cells and the bright dot like structures are GNPs localized within cells, respectively. **Figure 29 (C)** contains few spectra collected from GNP clusters localized within cells.

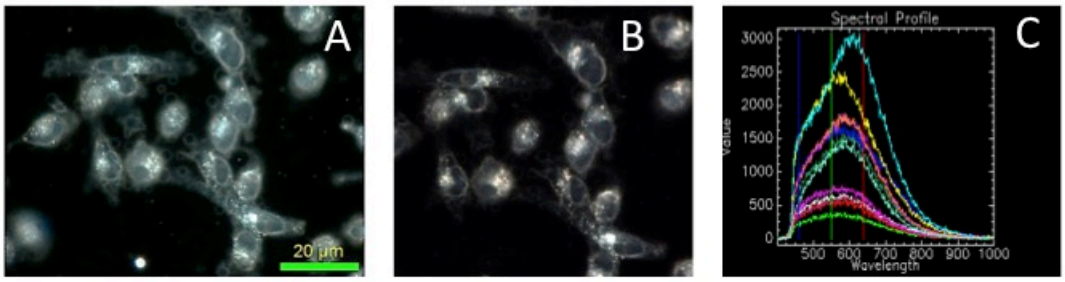

Figure 29. Dark-field and hyperspectral images of LNPs in cells. A) Dark-field image of MDA-MB-231 cells alone B) hyperspectral image of the same cells, and C) spectral profile of few GNP clusters localized within those cells. MDA-MB-231 cells.

4.4 Radiation Dose Enhancement

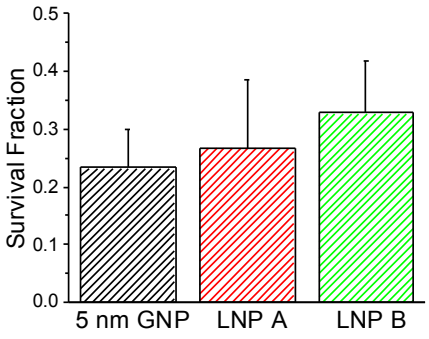

Figure 30. Dose enhancement of LNP**.** Survival fraction of cells following 2 Gy dose and internalization of 5 nm GNPs and LNPs.

After delivery of 2 Gy dose from 6 MV photons, the survival fraction of MDA-MB-231 cells was not significantly different with only 5 nm GNPs or LNPs encapsulating gold. This indicates that until optimization of GNP encapsulation is

completed to have a higher uptake of gold, there will not be any significant radiation dose enhancement. The damage to DNA was mapped using DNA double stand breaks (DSBs) assay to further verify the outcome of clonogenic experiment. DNA DSBs are the most lethal and mapping the DNA damage will be a useful indicator of the radiation damage to cells.

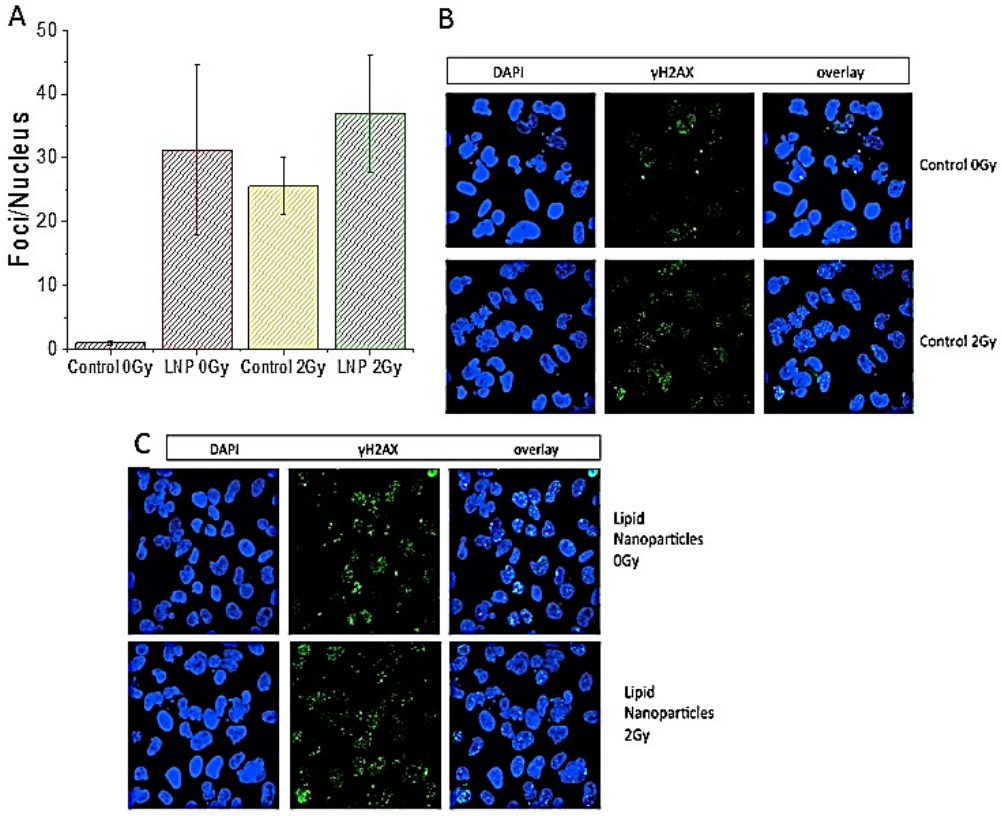

Figure 31. Mapping of DNA damage. A) Quantified DNA double strand breaks in cells treated with LNPs and radiation dose of 2 Gy, **B**) Qualitative images of DNA damage in control cells (with no GNPs) before (top panel) and after giving radiation dose of 2 Gy (bottom panel), and C) Qualitative images of DNA damage in cells treated with LNP-A before (top panel) and after giving radiation dose of 2 Gy (bottom panel). DAPI stains the nucleus (blue) of the cell and γH2AX localizes at sites of DSBs (green).

Figure 31 shows the DNA damage in cells treated with LNP formulation A and radiation. Because of toxicity issues discussed in section 4.2 results for only one LNP formulation are shown in **Figure 31.** The results are consistent with the data obtained

from clonogenic assay (see **Figure 30**). One method that radiation damages cells is by creation of DSBs in DNA. Cancer cells typically have some damaged DNA to begin with, which can be seen by the presence of γH2AX foci in the top control 0Gy panel in **Figure 31 (B)**. Radiation can produce additional DNA DSBs. When there is a DNA DSB, the repair proteins such as γH2AX are recruited to the damage site for repair process. Primary and secondary antibodies were used to map these repair proteins since they are indicators of DNA DSBs. The images for Control 2Gy show an increase in DSB compared to Control 0Gy as expected (see the bottom panel in **Figure 31** (**B**). However, LNPs without radiation also increased the number of double strand breaks significantly as shown in **Figure 31 C** (top panel). When LNPs were present and 2Gy radiation was delivered there was not a significant increase in double-strand breaks labeled with γH2AX antibody. This could be due to the fact that the number of GNPs internalized was not enough to cause significant radiation dose enhancement.

4.5 Discussion

Preliminary results showed LNP-A and LNP-B had a lower than expected encapsulation of GNPs with only of 1.5 ± 1.5 GNPs/LNP for formulation A and 5.0 ± 4.8 GNPs/LNP in formulation B. Although small 5nm GNPs were present inside the lipid nanoparticles as confirmed by TEM and hyperspectral imaging, the low number of GNPs per LNP and presence of empty LNPs limited the efficiency of GNP delivery to the cell. For example, there was not a great improvement in uptake over 5nm GNPs alone. Clonogenic results showed that LNPs induced toxicity when added at a concentration of 0.2 nM, however, it was an improvement in SF over 5 nm GNPs alone. After a 2 Gy dose of 6MV photons, LNPs in cells showed no significant enhancement of radiation sensitization. In order to evaluate the radiation dose enhancement due to NPs using clonogenic assay, the toxicity due to NPs should be lower. This way it could be argued that the reduced survival of cells can be due to the radiation induced damage. This result led us to explore another NP system to understand how cell synchronization affect uptake and radiation dose enhancement. The GNP complexes chosen were diameter 15 nm and 46 nm surface functionalized with both polyethylene glycol (PEG) and a peptide

containing integrin binding domain, RGD as discussed in the previous chapter.

Chapter 5
Results & discussion III: Synchronized cell population

5.1 Synchronization

Previous studies have established that properties of nanoparticles such as size, shape and surface functionalization can influence nanoparticle uptake by cells [70]. It is also known that radiation dose enhancement properties due to GNPs is also dependent on the size of GNPs [6]. However, it is not yet known how cellular uptake of GNPs and their radiation dose enhancement properties in a synchronous cell population compares to a control cell population where phase of each cell can vary. In this chapter, the influence of the cell cycle on cellular uptake of GNPs and their radiation dose enhancement properties is discussed in MDA-MB-231 breast cancer cells.

5.1.1 Cell phase verification

Figure 32 illustrates the variation of cell phase in a synchronous cell population as a function of time. In other words, **Figure 32** shows the number of counts *vs.* amount of DNA as a function of time in a synchronous cell population. It is known that the amount of DNA in a cell varies through its cycle. In G1 there is one copy of DNA (23 pairs of chromosomes in each human cell, 2n). During S phase DNA replication occurs, therefore there is somewhere between one and two copies of genetic material. Right before mitosis, the cell have two copies of DNA (4n) in G2. During mitosis, cell divide and each of the daughter cells (in G1) have 23 pairs of chromosomes, one copy of DNA (2n) again.

In **Figure 32,** the grey curve represents a control (asynchronous) population of cells. There are many cells in G1 since cells spend a long time in this phase growing and preparing. The dip between the two local maxima is all of the cells in S phase, and the second smaller maximum is representative of the cells in G2. The blue curve in **Figure 34** represents cell population immediately after the double-thymidine block synchronization process. The peak has shifted into S phase since thymidine inhibits DNA replication and arrests the cells in S phase.

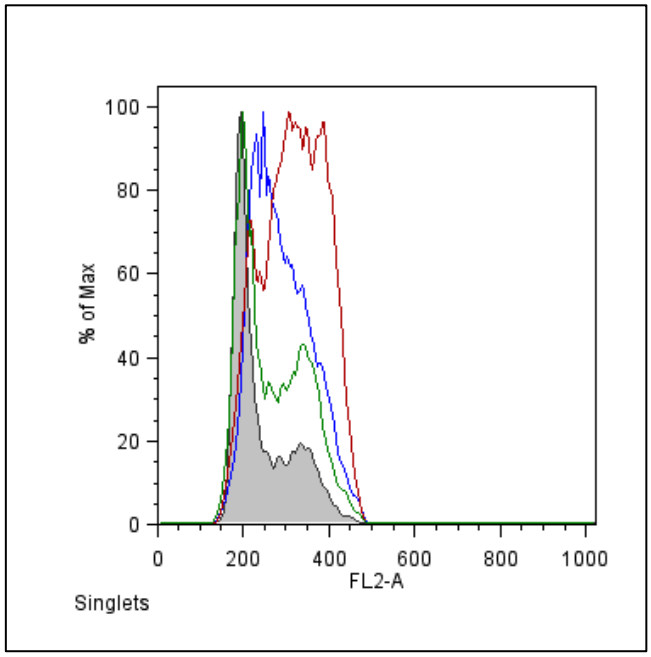

Figure 32. Cell cycle analysis. Quantification of amount of DNA per cell allowed identification of cell cycle phase. Grey curve represents control unsynchronized population. Blue curve represents the cell population immediately after synchronization (0 hours). Red curve shows the phase of cells after 3 hours of synchronization while green curve represent cell phase distribution after 20 hours of synchronization (the time of cell irradiation).

The blue curve clearly shows that the cell population is successfully synchronized. Just after synchronization new DMEM media was introduced and there a gap of 3 hours before the addition GNPs into MDA-MB-231 cells. The phase of cell population just before adding NPs was recorded and it is represented using the red curve in **Figure 32**. The cell population was in late S phase/G2 just before introduction of GNPs. The breast cancer cells were incubated with GNPs for 20 hours at a concentration of 0.2 nM before giving a radiation dose of 2 Gy. The green curve shows our cell population at the time of radiation and part of the population was in G1 again with a fraction also in G2. It is likely the cells arrested in late S phase have already had the chance to complete mitosis and divide while the rest of the population was still preparing for mitosis.

5.1.2 Uptake in synchronized population

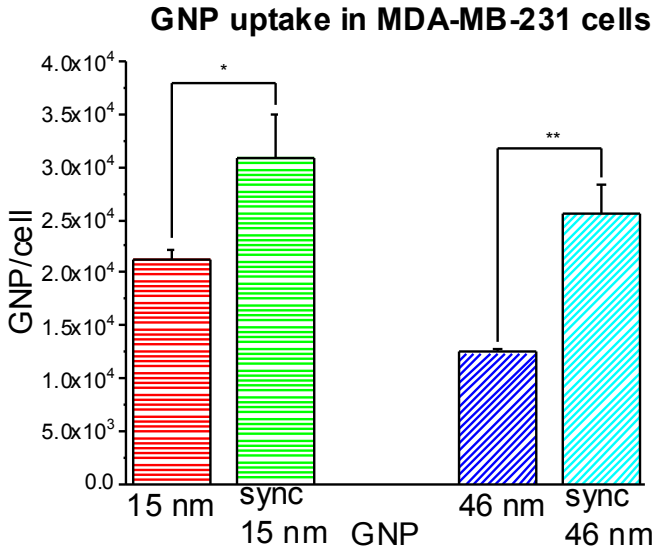

Figure 33. Uptake of 15 nm and 46 nm GNPs in control and synchronized cell population of MDA-MB-231.

As illustrated in **Figure 33**, GNP uptake for both nanoparticle sizes improved in the synchronous cell population as compared to control (asynchronous) one. For 15 nm PEG/RGD nanoparticles, uptake increased from 21348 ± 924 GNP/cell to 30848 ± 4000 GNP/cell and it was a 1.5-fold increase in the synchronous cell population compared to the control. In the case of 46 nm GNPs, there was a 2-fold increase in NP uptake and number of GNPs per cell was increased from 12424 ± 430 to 25599 ± 2783 GNP/cell in the synchronized cell population *vs.* control. The increase in uptake of GNPs per cell was determined to be statistically significant for synchronized populations of MDA-MB-231 cells incubated with both 15 nm GNPs and 46 nm GNPs (* = $p<0.05$, ** = $p<0.01$).

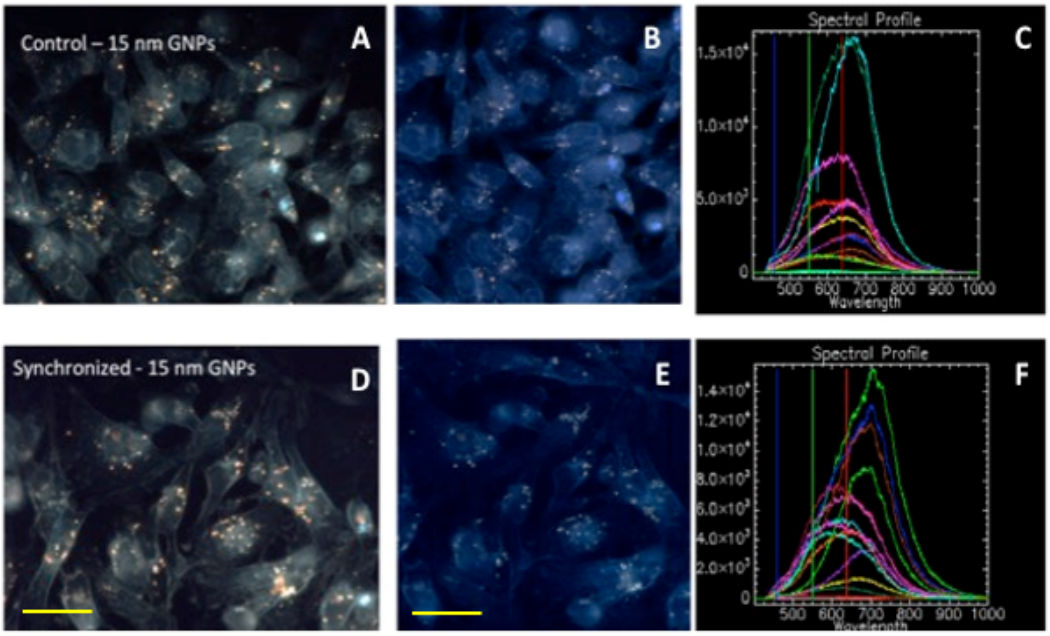

Figure 34. Dark-field and hyperspectral images of GNPs in cells. GNPs of size 15 nm in an asynchronous (A-C) and synchronous (D-F) MDA-MB-231 cells. The left, middle, and right most columns represents dark-field, hyperspectral, and few spectra collected from GNP clusters localized within cells. The scale bar is 20 µm.

Figure 34 shows that GNPs were internalized within MDA-MB-231 cells and the bright structures in those cells represent GNP clusters localized within cells as pointed out before in chapter 4. The cells were grown on glass coverslips and incubated with NPs for 20 hours in order to facilitate their imaging with CytoViva optical microscope. **Figure 23** shows the dark-field and hyperspectral images of *individual GNPs* is around 600 nm. However, the peak for GNPs localized within cells is around 650. The reflectance spectra collected shows a clear red shift as a result of their aggregation within these vesicles. For example, GNPs enters cells *via* receptor mediated endocytosis process and get trapped in endosomes and lysosomes before they get excreted from the cells. Studies have shown that GNPs get aggregated in those vesicles due to change in the pH [34].

5.2 Radiation dose enhancement

It is still not known how radiation dose enhancement due to GNPs would change in a synchronous cell population vs. a control one. As discussed in the previous section there is a significant increase in GNP uptake in a synchronous cell population *vs.* control one. Our next goal was to determine how this change in uptake translated into radiation dose enhancement due to these NPs.

5.2.1 Effect of synchronization on cell population incubated with 15 nm gold nanoparticles

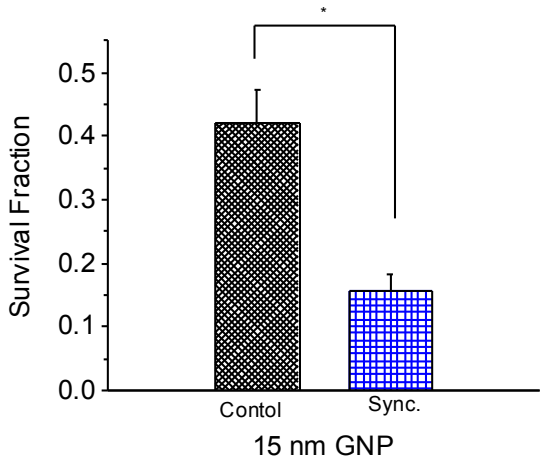

Figure 35. Survival Fraction after 2Gy dose and incubation with 15 nm GNPs, of MDA-MB-231 control and synchronized cell populations.

Variation in radiation dose enhancement due to 15 nm GNPs in a synchronous and control cell populations was assessed using clonogenic assay and the results are shown in **Figure 35**. The MDA-MB-231 cell population that was synchronized prior to incubation with 15 nm GNPs functionalized with PEG/RGD showed a 63% decrease survival compared to control (unsynchronized) cells after receiving a radiation dose of 2Gy. Survival fractions were determined to be 0.42 ± 0.05 for control and 0.16 ± 0.03 for synchronized cells, this difference is statistically significant ($p<0.05$).

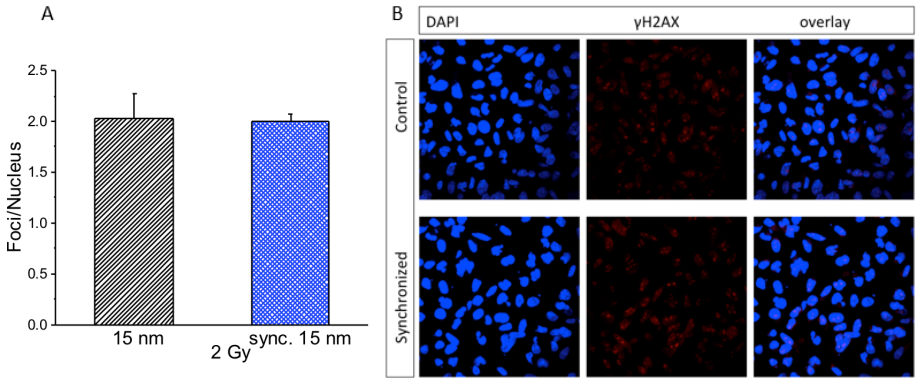

Figure 36. Comparison of DNA damage. A-B) Qualitative and quantitative presentation of DNA DSBs in control and synchronized population of MDA-MB-231 cells after a radiation dose of 2 Gy, respectively. One of the repair proteins, γH2AX, was probed in this study. Size of the GNPs used was 15 nm.

MDA-MB-231 cells incubated with 15 nm PEG/RGD GNPs for 20 hours were irradiated with 2 Gy of 6 MV photons and then fluorescently tagged with DAPI and γH2AX antibodies 24 hours after treatment. Qualitative and quantitative data corresponding to DNA-DSBs is illustrated in **Figure 36**. Nucleus was stained with DAPI and it is shown in blue in the image panel A while γH2AX foci are shown in red. Quantitative data was collected by counting γH2AX foci and dividing by the number of nuclei in the image. There were 2.0 ± 0.2 foci/nucleus for the control-unsynchronized population and 2.0 ± 0.1 foci/nucleus when cell cycles are synchronized. These are almost identical. This could indicate that there is another mechanism damaging cells, besides DNA double-strand breaks. These nanoparticle systems do not enter the nucleus of the cell, so maybe increased uptake in synchronized population is having an effect on other cellular functions such as cytoskeleton, or other organelles. Or differences are not present 24 hours later, but at a longer time point, which is why a difference is observed in a clonogenic assay result that ends 14 days after irradiation of cells.

It has been discussed how synchronization of cells affect radiation dose enhancement due to 15 nm GNPs functionalized with PEG and RGD peptide. In the next section data corresponding to 46 nm GNPs functionalized similarly is presented.

5.2.2. Effect of synchronization on cell population incubated with 46 nm GNPs

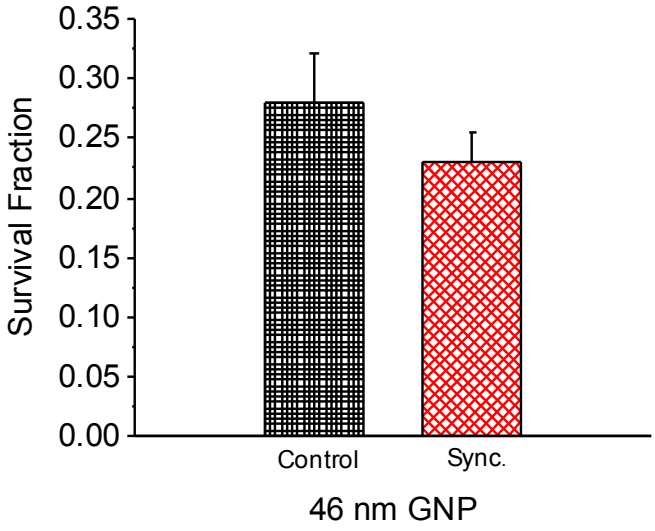

Figure 37. Comparison of cell survival fraction for control and synchronized MDA-MB-231 cells with 46 nm GNPs.

As shown in **Figure 37**, a synchronized population of MDA-MB-231 cells had an 18% decrease in cell survival compared to unsynchronized cells incubated with 0.2 nM of 46 nm PEG/RGD GNPs. The survival fraction was changed from 0.28 ± 0.04 to 0.23 ± 0.03 for control and synchronized population, respectively.

DNA DSBs assay in addition to clonogenic assay were performed to evaluate the damage due to radiation treatment in the presence of GNPs as illustrated in **Figure 38**. Coverslips with MDA-MB-231 cells were fluorescently stained, then imaged and analyzed. DAPI was used to stain the nucleus of the cell and a γH2AX antibody stained DNA double-strand break sites. Images were quantified by counting an average number of γH2AX foci per nucleus. In the control cell population, there were 2.9 ± 0.5 foci per nucleus while it was 2.9 ± 0.4 foci/nucleus in synchronized cell population. There was no difference in DSB per cell when GNPs were added to control or a synchronized cell population.

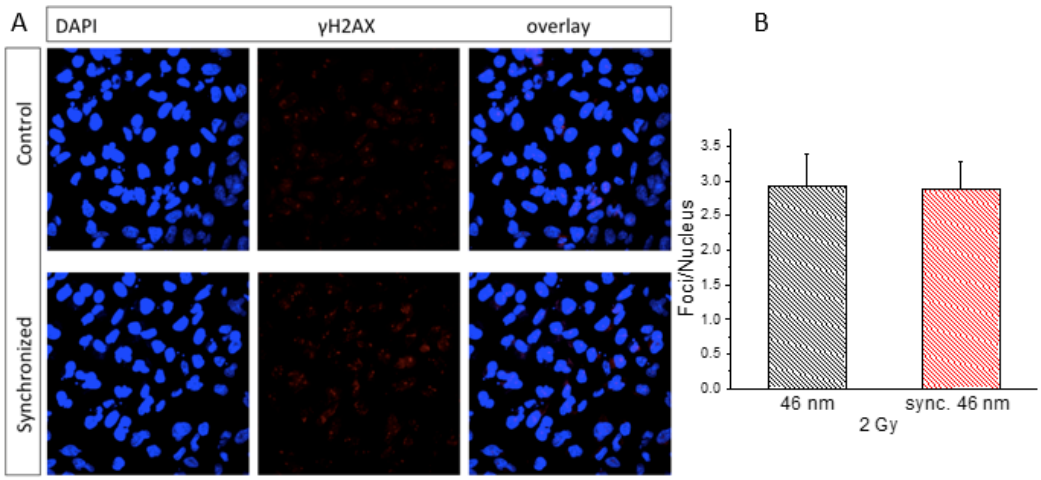

Figure 38. Comparison of gammaH2AX foci (DNA DSBs) per nucleus in control and synchronized populations of MDA-MB-231 breast cancer cells following uptake of 46 nm GNPs.

5.3 Discussion

Radiation therapy is an important tool when it comes to the treatment of cancer. Despite advancements in development of new modalities, it continues to be a challenge to deliver a curative dose to tumour tissue while sparing the surrounding normal tissue. Radiation sensitization of tumour cells by specifically delivering high-Z material such as GNPs, would shift a dose response curve enough that perhaps a lower radiation dose could be used while minimizing damage to normal tissues.

One of the common protocols in radiation therapy treatment involves giving many small dose fractions. For example, many fractions of 1.8 - 2 Gy daily dose, 5 fractions per week leading up to an overall dose of 40-70 Gy depending on the tumour size, localization and histology. Therefore in this study, I investigated the effects seen after a 2 Gy dose to evaluate the dose enhancement due to GNPs per fraction. The radiation beam used was a 6 MV photon beam from a Varian linear accelerator at BC Cancer. This is a common energy used in clinic, however, lower energy beams would have a greater interaction with gold, and they have less penetration in an actual patient and also have a skin sparing effect. Previous biological study by Jain *et al.* found comparable sensitization in MV energy range in MDA-MB-231 cells at 12 μM concentration with 1.9

nm GNPs [71, 72]. The dose enhancement ratio of 1.29 was reported for that study. However, the concentration used was in micro-molar range and it would be very difficult to reach such high concentration of GNPs within the tumour *in vivo*. Monte Carlo simulation study by Cho *et al.* simulated the dose enhancement for 6 MV photons and found tumour dose enhancements was lower than the experimentally observed [25]. Some of the biological interactions are difficult to mimic in theoretical calculations, however, the trends were the same for both experimental and theoretical studies based on GNP-mediated sensitization. Experiments for this thesis were carried out in nano-molar concentrations, which is 1000 times less than what Jain *et al.* used for their study. Therefore based on previous studies that used higher concentrations of gold, it should be feasible to reach such concentrations *in vivo* [73]. In addition, larger GNPs of 15 nm and 46 nm were used for this study instead of 1.9 nm GNPs.

Previous studies have shown that 50 nm (as-made) GNPs have a higher uptake at monolayer level while smaller GNPs are able to pass through the extra-cellular matrix once they leave the tumour blood vessels [34, 62]. However, these NPs were functionalized with PEG and RGD peptide so that they could be used in an animal model and NPs will have an improved uptake once they reach individual cells. It was found that both of these two sizes of NPs enter tumour cells better in a synchronized cell population and produced higher dose enhancement. When the cells were synchronized, NP uptake was increased 1.5-2 times. Kim *et al.* were able to show that nanoparticle uptake is influenced by the cell cycle phase, with greatest uptake occurring in G2/M phase [70]. Based on the timing of the experiment most of the cells progress into G2/M phase when nanoparticles were added as shown in **Figure 34**. Hence, one possibility is that most of the cell population was in a state where the membrane and receptor-mediated endocytosis were efficient at the point of GNP incubation and as a result uptake was improved.

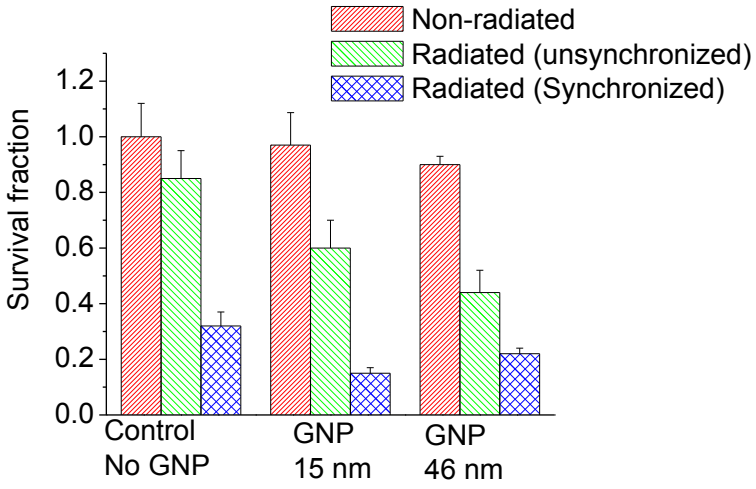

Figure 39. Survival fraction summary for MDA-MB-231 cells, showing decrease in cell survival when population is synchronized.

Figure 39 shows the summary of radiation study done with 15 and 46 nm GNPs. With synchronized cells, survival fraction for and 15 nm and 46 nm PEG/RGD GNPs was 0.23 ± 0.07 and 0.34 ± 0.02. A 40% and 15% decrease. It is well established that the primary target of radiation therapy is nuclear DNA, with double-strand breaks being the most lethal form of damage; however, evidence shows that radiation damage to mitochondria and cell membrane may contribute to cytotoxic effect of radiation and may be a mechanism affecting results in this experimental set-up [46].

As illustrated in **Figures 36** and **38,** although there was a difference in survival when the cell population was synchronized *vs.* unsynchronized, the amount of additional double-strand breaks was the same for synchronized and control populations of MDA-MB-231 cells. Hence, another mechanism could be having an effect. Our research group will conduct these studies in the future.

Chapter 6
Conclusion

GNPs have great potential to use as radiation dose enhancers in radiation therapy treatments. To be effective, however, GNPs must be delivered to and internalized by cancer cells since the range of electrons produced by GNPs in the presence of a radiation beam is small. Previous studies showed that physicochemical peripheries of GNPs could influence their uptake. The work described in this thesis went one step further and extended previous work to explore how uptake and radiation dose enhancement of GNPs change in a synchronous cell population *vs.* an asynchronous (control) one. In order to achieve that different sized GNP systems were delivered to both synchronized and control MDA-MB-231 cell populations followed by a 2 Gy radiation dose using 6 MV photons to quantify the radiation dose enhancement.

Lipid nanoparticles (LNPs) encapsulating small 5 nm GNPs were investigated as a way to take advantage of the energetically favourable 50 nm size of particle. Internalization of GNPs was limited due to minimal encapsulation of GNP/LNP, with only approximately 1-5 GNP/LNP. This resulted in a very low dose radiation dose enhancement. It was also seen that there was some toxicity introduced even at a concentration of 0.2 LNP/ml. Future plans for our group are to improve these LNP-based systems for their use in future experiments. The GNPs of diameter 15 nm and 46 nm were introduced to test whether there is a difference in uptake and resulting radiation dose enhancement in a synchronous *vs.* asynchronous cell populations.

GNPs of two different sizes (15 nm and 46 nm) were functionalized with PEG/RGD and incubated with MDA-MB-231 cells for 20 hours. Uptake was found to differ between sizes, with 15nm GNPs showing greater accumulation in cells. The cell population was synchronized by double-thymidine block prior to addition of GNPs uptake of GNPs and the uptake of GNPs was increased 1.5-2 fold.

Fluorescent imaging able to identify double strand breaks post-irradiation and help quantify DNA damage enhancement. Although there was a difference in cell survival when synchronized population was given a radiation dose of 2 Gy, the difference in DNA double strand breaks labeled by γH2AX primary and secondary antibodies

remained statistically not significant. This suggests there could be another mechanism of cell damage.

It is recognized that *in vitro* data cannot be extrapolated directly into *in vivo* or clinical settings because things such as the tumour microenvironment and that tumours contain heterogeneous cell populations with varying sensitivity to radiation are not accounted for. As shown in table 3, small differences in cell survival can translate to large differences and greater significance during a course of multiple treatments [74]. The experimental survival fraction (X), was propagated through 30 fractions (X^{30}) and the number of surviving cells for a tumour containing 10^{12} cells estimated. This really highlights how small differences in survival can translate into large differences over multiple treatments.

The probability of tumour control can be estimated from the following equation:

$$P_o = e^{-a}$$

Where P_0 is the probability that the tumour will contain no survival stem cells and a is the average number of surviving cells [74]. Tumour stem cells are the limited proportion of tumour cells with the capacity for cell proliferation [74]. A smaller change in survival fraction after one dose could lead to a significant improvement in the number of surviving cells and therefore the tumour control probability. For example, improvement estimated here was 9-fold for 15 nm GNPs and 249-fold for 50 nm GNPs.

Table 2. Possible improvement of radiation sensitization with GNPs in fractionated delivery to tumour

	Experimental survival fraction (X)	SF post 30 (n) treatment (X^n)	Average number of cells surviving for a tumor containing 10^{12} cells	Improvement factor when compared to control
Control (no GNPs)	0.42	4.98×10^{-12}	4.98	1
15 nm GNPs	0.39	5.39×10^{-13}	0.53	9.33
50 nm GNPs	0.35	2.01×10^{-14}	0.02	249

The goal of this work was to explore how cell cycle influences NP uptake. The results presented here are bringing us closer to understanding radiation enhancement achieved with GNPs and optimization techniques that could be useful when implemented in clinic. A recent study has shown that outcome of radiation therapy can be improved by controlling the cell cycle [59]. Hence introduction of GNPs into cell-cycle-controlled tumours could generate significant improvement in radiation therapy. Cancer nanotechnology will have a significant impact in future cancer therapy. Targeting of cancer therapeutics to tumours would not only reduce side effects to patients but will improve the quality of life.

Bibliography

1. Ruddon, R.W. and MyiLibrary, *Cancer biology*. 4th ed. 2007, New York;Oxford;: Oxford University Press.
2. Joiner, M. and A. van der Kogel, *Basic Clinical Radiobiology*. 2009, Taylor and Francis Group 6000 Broken Sound Parkway, NW, Suite 300 Boca Raton, FL 33487-2742 CRC Press.
3. Arthur, D.W., et al., *Short Course Breast Radiotherapy: A Comprehensive Review of Hypofractionation, Partial Breast, and Intra-Operative Irradiation*. 1st 2016. ed. 2016, Cham: Springer International Publishing.
4. Chang, D.S., et al., *Basic Radiotherapy Physics and Biology*. 2014 ed. 2014, Cham: Springer International Publishing.
5. Cho, S.H. and S. Krishnan, *Cancer nanotechnology: principles and applications in radiation oncology*. 2013, Boca Raton, FL: CRC Press.
6. Chithrani, D.B., et al., *Gold Nanoparticles as Radiation Sensitizers in Cancer Therapy.* Radiation Research, 2010. **173**(6): p. 719-728.
7. Khadem Abolfazli, M., S.R. Mahdavi, and G. Ataei, *Studying Effects of Gold Nanoparticle on Dose Enhancement in Megavoltage Radiation.* Journal of biomedical physics & engineering, 2015. **5**(4): p. 185-190.
8. Baskar, R., et al., *Cancer and Radiation Therapy: Current Advances and Future Directions.* INTERNATIONAL JOURNAL OF MEDICAL SCIENCES, 2012. **9**(3): p. 193-199.
9. Indelicato, P. and A. Karpov, *Sizing up atoms: Theoretical physics.* Nature, 2013. **498**(7452): p. 40-41.
10. Mayles, P., et al., *Handbook of radiotherapy physics: theory and practice*. 1 ed. 2007, New York: Taylor & Francis.
11. Plopper, G., et al., *Lewin's cells*. Third ed. 2015, Burlington, MA: Jones & Bartlett Learning.
12. Meyers, R.A., *Encyclopedia of molecular cell biology and molecular medicine*. 2nd ed. 2004, Weinheim, Germany: Wiley-VCH.
13. Waite, G.N. and L. Waite, *Applied cell and molecular biology for engineers*. 2007, New York: McGraw-Hill.
14. Ciccia, A. and S.J. Elledge, *The DNA Damage Response: Making It Safe to Play with Knives.* Molecular Cell, 2010. **40**(2): p. 179-204.
15. McMahon, S.J., et al., *Nanodosimetric effects of gold nanoparticles in megavoltage radiation therapy.* RADIOTHERAPY AND ONCOLOGY, 2011. **100**(3): p. 412-416.
16. Willers, H., J. Dahm-Daphi, and S.N. Powell, *Repair of radiation damage to DNA.* British Journal Of Cancer, 2004. **90**: p. 1297.
17. Pharoah, P.D.P., et al., *Normal tissue reactions to radiotherapy: towards tailoring treatment dose by genotype.* Nature Reviews Cancer, 2009. **9**(2): p. 134-142.

18. Matsudaira, H., A.M. Ueno, and I. Furuno, *Iodine Contrast Medium Sensitizes Cultured Mammalian Cells to X Rays but Not to γ Rays.* Radiation Research, 1980. **84**(1): p. 144-148.
19. Iwamoto, K.S., et al., *Radiation dose enhancement therapy with iodine in rabbit VX-2 brain tumors.* Radiotherapy and Oncology, 1987. **8**(2): p. 161-170.
20. Nath, R., P. Bongiorni, and S. Rockwell, *IODODEOXYURIDINE RADIOSENSITIZATION BY LOW-ENERGY AND HIGH-ENERGY PHOTONS FOR BRACHYTHERAPY DOSE-RATES.* RADIATION RESEARCH, 1990. **124**(3): p. 249-258.
21. Xie, W.Z., et al., *Simulation on the molecular radiosensitization effect of gold nanoparticles in cells irradiated by x-rays.* PHYSICS IN MEDICINE AND BIOLOGY, 2015. **60**(16): p. 6195-6212.
22. Hainfeld, J.F., D.N. Slatkin, and H.M. Smilowitz, *The use of gold nanoparticles to enhance radiotherapy in mice.* Physics in Medicine and Biology, 2004. **49**(18): p. N309-N315.
23. Dimitriou, N.M., et al., *Gold nanoparticles, radiations and the immune system: Current insights into the physical mechanisms and the biological interactions of this new alliance towards cancer therapy.* Pharmacology and Therapeutics, 2017. **178**: p. 1-17.
24. Rosa, S., et al., *Biological mechanisms of gold nanoparticle radiosensitization.* Cancer nanotechnology, 2017. **8**(1): p. 2.
25. Mesbahi, A., *A review on gold nanoparticles radiosensitization effect in radiation therapy of cancer.* Reports of Practical Oncology and Radiotherapy, 2010. **15**(6): p. 176-180.
26. Carter, J.D., et al., *Nanoscale energy deposition by x-ray absorbing nanostructures.* JOURNAL OF PHYSICAL CHEMISTRY B, 2007. **111**(40): p. 11622-11625.
27. Her, S., D.A. Jaffray, and C. Allen, *Gold nanoparticles for applications in cancer radiotherapy: Mechanisms and recent advancements.* Advanced Drug Delivery Reviews, 2017. **109**: p. 84-101.
28. Nel, A., et al., *Toxic Potential of Materials at the Nanolevel.* Science, 2006. **311**(5761): p. 622-627.
29. Butterworth, K.T., et al., *Physical basis and biological mechanisms of gold nanoparticle radiosensitization.* Nanoscale, 2012. **4**(16): p. 483-4838.
30. Pan, Y., et al., *Gold Nanoparticles of Diameter 1.4 nm Trigger Necrosis by Oxidative Stress and Mitochondrial Damage.* SMALL, 2009. **5**(18): p. 2067-2076.
31. Pawlik, T.M. and K. Keyomarsi, *Role of cell cycle in mediating sensitivity to radiotherapy*. 2004, Elsevier Inc: NEW YORK. p. 928-942.
32. Butterworth, K.T., et al., *Evaluation of cytotoxicity and radiation enhancement using 1.9 nm gold particles: potential application for cancer therapy.* Nanotechnology, 2010. **21**(29): p. 295101.
33. Maeda, H., *Macromolecular therapeutics in cancer treatment: The EPR effect and beyond.* Journal of Controlled Release, 2012. **164**(2): p. 138-144.

34. Chithrani, B.D., A.A. Ghazani, and W.C.W. Chan, *Determining the size and shape dependence of gold nanoparticle uptake into mammalian cells.* Nano letters, 2006. **6**(4): p. 662-668.
35. Cruje, C., et al., *Optimization of PEG coated nanoscale gold particles for enhanced radiation therapy.* RSC Advances, 2015. **5**(123): p. 101525-101532.
36. Manson, J., et al., *Polyethylene glycol functionalized gold nanoparticles: the influence of capping density on stability in various media.* Gold Bulletin - Journal Article, 2011. **44**(2): p. 99-105.
37. Yang, C., K. Bromma, and D. Chithrani, *Peptide Mediated In Vivo Tumor Targeting of Nanoparticles through Optimization in Single and Multilayer In Vitro Cell Models.* CANCERS, 2018. **10**(3): p. 84.
38. Yin, H.Q., F.L. Bi, and F. Gan, *Rapid Synthesis of Cyclic RGD Conjugated Gold Nanoclusters for Targeting and Fluorescence Imaging of Melanoma A375 Cells.* BIOCONJUGATE CHEMISTRY, 2015. **26**(2): p. 243-249.
39. Chithrani, B.D., et al., *Intracellular uptake, transport, and processing of nanostructures in cancer cells.* Nanomedicine: Nanotechnology, Biology and Medicine, 2009. **5**(2): p. 118-127.
40. Jin, H., D.A. Heller, and M.S. Strano, *Single-particle tracking of endocytosis and exocytosis of single-walled carbon nanotubes in NIH-3T3 cells.* NANO LETTERS, 2008. **8**(6): p. 1577-1585.
41. Dichello, G.A., et al., *Preparation of liposomes containing small gold nanoparticles using electrostatic interactions.* European Journal of Pharmaceutical Sciences, 2017. **105**: p. 55-63.
42. Shah, R., et al., *Lipid Nanoparticles: Production, Characterization and Stability*. 2015 ed. 2015, Cham: Springer International Publishing.
43. Frens, G., *Controlled nucleation for the particle size in monodisperse gold suspensions.* Nature, 1973. **241**: p. 20-22.
44. Wu, P.H., et al., *Targeting integrins with RGD-conjugated gold nanoparticles in radiotherapy decreases the invasive activity of breast cancer cells.* INTERNATIONAL JOURNAL OF NANOMEDICINE, 2017. **12**: p. 5069-5085.
45. Haiss, W., et al., *Determination of size and concentration of gold nanoparticles from UV-Vis spectra.* ANALYTICAL CHEMISTRY, 2007. **79**(11): p. 4215-4221.
46. Prise, K.M., et al., *New insights on cell death from radiation exposure.* Lancet Oncology, 2005. **6**(7): p. 520-528.
47. Schultz, R.A., et al., *Hyperspectral imaging: A novel approach for microscopic analysis.* Cytometry, 2001. **43**(4): p. 239-247.
48. Badireddy, A.R., M.R. Wiesner, and J. Liu, *Detection, Characterization, and Abundance of Engineered Nanoparticles in Complex Waters by Hyperspectral Imagery with Enhanced Darkfield Microscopy.* ENVIRONMENTAL SCIENCE & TECHNOLOGY, 2012. **46**(18): p. 10081-10088.
49. Zamora-Perez, P., et al., *Hyperspectral-Enhanced Dark Field Microscopy for Single and Collective Nanoparticle Characterization in Biological Environments.* Materials, 2018. **11**(2).
50. Whitfield, M.L., et al., *Identification of genes periodically expressed in the human cell cycle and their expression in tumors.* Molecular biology of the cell, 2002. **13**(6): p. 1977-2000.

51. Crissman, H.A. and J.A. Steinkamp, *Rapid, Simultaneous Measurement of DNA, Protein, and Cell Volume in Single Cells from Large Mammalian Cell Populations.* The Journal of Cell Biology, 1973. **59**(3): p. 766-771.
52. Krishan, A., *Rapid Flow Cytofluorometric Analysis of Mammalian Cell Cycle by Propidium Iodide Staining.* The Journal of Cell Biology, 1975. **66**(1): p. 188-193.
53. Stoeva, S.I.P., B.L.V.; Uma, Sitharaman; Stoimenov, Peter K.; Zaikovski, Vladimir; Sorensen, Christopher M.; Klabunde, Kenneth J., *Face-Centered Cubic and Hexagonal Closed-Packed Nanocrystal Superlattices of Gold Nanoparticles Prepared by Different Methods.* J. PHys. Chem. B, 2003. **107**: p. 7441-7448.
54. Butcher, D.J. and J. Sneddon, *A practical guide to graphite furnace atomic absorption spectrometry*. Vol. 149;149.;. 1998, New York: Wiley.
55. Ebdon, L. and E.H. Evans, *An introduction to analytical atomic spectrometry*. 1998, Chichester, England;New York;: John Wiley.
56. Blumenthal, R.D., *Chemosensitivity*. Vol. 110-111. 2005, Totowa, N.J: Humana Press.
57. Cruje, C. and B.D. Chithrani, *Integration of Peptides for Enhanced Uptake of PEGylayed Gold Nanoparticles.* Journal of Nanoscience and Nanotechnology, 2015. **15**(3): p. 2125-2131.
58. Stetefeld, J., S.A. McKenna, and T.R. Patel, *Dynamic light scattering: a practical guide and applications in biomedical sciences.* Biophysical Reviews, 2016. **8**(4): p. 409-427.
59. Pan, Y., et al., *Size-dependent cytotoxicity of gold nanoparticles.* SMALL, 2007. **3**(11): p. 1941-1949.
60. Trono, J.D., et al., *Size, Concentration and Incubation Time Dependence of Gold Nanoparticle Uptake into Pancreas Cancer Cells and its Future Application to X-ray Drug Delivery System.* Journal of Radiation Research, 2011. **52**(1): p. 103-109.
61. Darren Yohan Charmainne Cruje Xiaofeng Lu Devika, C., *Elucidating the Uptake and Distribution of Nanoparticles in Solid Tumors via a Multilayered Cell Culture Model.*, 2015. **7**(2): p. 127-137.
62. Darren Yohan Charmainne Cruje Xiaofeng Lu Devika, B.C., *Size-Dependent Gold Nanoparticle Interaction at Nano–Micro Interface Using Both Monolayer and Multilayer(Tissue-Like) Cell Models*, 2016. **8**(1): p. 44-53.
63. Kang, J.H. and Y.T. Ko, *Lipid-coated gold nanocomposites for enhanced cancer therapy.* INTERNATIONAL JOURNAL OF NANOMEDICINE, 2015. **10**: p. 33-45.
64. Von White, n.G., et al., *Structural and thermal analysis of lipid vesicles encapsulating hydrophobic gold nanoparticles.* ACS nano, 2012. **6**(6): p. 4678-4685.
65. Baowan, D. and N. Thamwattana, *Modelling encapsulation of gold and silver nanoparticles inside lipid nanotubes.* Physica A: Statistical Mechanics and its Applications, 2014. **396**: p. 149-154.
66. Lee, P., et al., *Enhancement of anticancer efficacy using modified lipophilic nanoparticle drug encapsulation.* INTERNATIONAL JOURNAL OF NANOMEDICINE, 2012. **7**: p. 731-737.

67. Ray, T.R., et al., *Quantitative Characterization of the Colloidal Stability of Metallic Nanoparticles Using UV-vis Absorbance Spectroscopy.* LANGMUIR, 2015. **31**(12): p. 3577-3586.
68. Müller, R.H., K. Mäder, and S. Gohla, *Solid lipid nanoparticles (SLN) for controlled drug delivery – a review of the state of the art*. 2000, Elsevier B.V: AMSTERDAM. p. 161-177.
69. Kulkarni, J.A., P.R. Cullis, and R. van der Meel, *Lipid Nanoparticles Enabling Gene Therapies: From Concepts to Clinical Utility.* NUCLEIC ACID THERAPEUTICS, 2018. **28**(3): p. 146-157.
70. Kim, J.A., et al., *Role of cell cycle on the cellular uptake and dilution of nanoparticles in a cell population.* Nature Nanotechnology, 2012. **7**(1): p. 62-68.
71. Ghita, M., et al., *A mechanistic study of gold nanoparticle radiosensitisation using targeted microbeam irradiation.* SCIENTIFIC REPORTS, 2017. **7**(1): p. 44752.
72. Jain, S.M.B.B.C., et al., *Cell-Specific Radiosensitization by Gold Nanoparticles at Megavoltage Radiation Energies.* International Journal of Radiation Oncology, Biology, Physics, 2011. **79**(2): p. 531-539.
73. Zhang, X.-D., et al., *Toxicologic effects of gold nanoparticles in vivo by different administration routes.* International journal of nanomedicine, 2010. **5**: p. 771-781.
74. Tannock, I., *The basic science of oncology*. 4th ed. 2005, New York: McGraw-Hill, Medical Pub. Division. xi, 555 p.